TECHNISCHE UNIVERSITÄT DRESDEN

Validating Sherpa for New Physics Simulations in Diboson Processes

Master-Arbeit
zur Erlangung des Hochschulgrades
Master of Science
im Master-Studiengang Physik

vorgelegt von

MAREN BÜHRING
geboren am 24.09.1998 in Hannover

Institut für Kern- und Teilchenphysik
Fakultät Physik
Bereich Mathematik und Naturwissenschaften
Technische Universität Dresden

2023

Eingereicht am 07. Dezember 2023

1. Gutachter: Dr. Frank Siegert
2. Gutachter: Prof. Dr. Arno Straessner

Summary

Abstract:
The Monte Carlo event generator Sherpa [1] enables the simulation of high-energy particle collisions, like the ones recorded by the ATLAS detector at the Large Hadron Collider (LHC). The simulations allow comparisons between the experimental data and a theoretical expectation. One of Sherpa's features is its compatibility with models formulated in the Universal FeynRules Output (UFO) format [2]. These UFO models enable simulations based on physics beyond the Standard Model (SM) of particle physics. This thesis performs validation tests for two seperate UFO models: The SMEFTsim model [3] is tested in the context of a Vector Boson Scattering process, and the HHVBF_UFO model [4] is tested using a process involving a triple Higgs coupling. The tests are based on consistency within Sherpa, as well as comparisons with events generated with the MadGraph5_aMC@NLO [5] event generator. While the validation results for the SMEFTsim model show good agreement with only one exception, the results for the HHVBF_UFO validation show discrepancies that need to be investigated further to rule out a possible inconsistency in Sherpa's handling of the UFO model.

Zusammenfassung:
Der Monte Carlo Event Generator Sherpa [1] erlaubt die Simulation von hochenergetischen Teilchenkollisionen, wie sie zum Beispiel vom ATLAS Detektor am Large Hadron Collider (LHC) gemessen werden. Die Simulationen machen Vergleiche zwischen theoretischen Vorhersagen und experimentellen Ergebnissen möglich. Eine Eigenschaft von Sherpa ist die Kompatibilität mit Modellen, die im Universal FeynRules Output (UFO) Format formuliert wurden. Diese UFO Modelle erlauben Simulationen die auf physikalischen Modellen jenseits des Standardmodells der Teilchenphysik beruhen. In dieser Arbeit werden Validierungen mit zwei verschiedenen UFO Modellen durchgeführt: Das SMEFTsim Modell [3] wird im Kontext eines Vektorbosonenstreuprozesses getestet, während das HHVBF_UFO Modell [4] mithilfe eines Prozesses getestet wird, der eine Dreifach-Higgskopplung enthält. Die Tests basieren einerseits auf Konsistenz innerhalb von Sherpa und andererseits auf Vergleichen mit dem Event Generator MadGraph5_aMC@NLO [5]. Während die Validierungen anhand des SMEFTsim Modells bis auf eine Ausnahme gute Übereinstimmungen zeigen, sind in der Validierung mithilfe des HHVBF_UFO Modells Unterschiede sichtbar, die weiter untersucht werden müssten, um eine Inkonsistenz in Sherpas Umgang mit dem UFO Modell auszuschließen.

Contents

1 Introduction

The Standard Model of Particle Physics (SM) is one of the great success stories within physics as a whole. It manages to accurately describe a wide range of experimental results from a long line of different experiments. Most recently, the ATLAS [6] and CMS [7] experiments at the Large Hadron Collider (LHC) [8] have delivered experimental evidence for the existence of the Higgs boson [9], further confirming the accuracy of the model in the experimentally available energy range. Despite this overwhelming success, the SM is known to be incomplete. It offers no explanations for the nature of dark matter or dark energy, and there has been no fully successful unification of the descriptions of gravity, which is based on Einstein's theory of general relativity, and the SM, which describes electromagnetism and the strong and weak interactions. There is no widely accepted explanation for baryon anti-baryon asymmetry, and there are still open questions with regard to neutrino masses.

This leads to an interesting disconnect: On the one hand, the SM accurately predicts almost all measurements produced by the available particle physics experiments. On the other hand, according to both cosmology and the potential inconsistencies of the SM itself, beyond SM (or BSM) physics appears to be out there. One possible explanation for this phenomenon is the energy scale of that new physics. It might be just, or way out of reach of the current state-of-the-art experiments (like the LHC). In that case, building colliders with higher centre of mass energies might reveal the discrepancies between the current SM and those future experimental results. Alternatively, or until then, one of the remaining options are high-precision measurements. If there is new physics at very high energies, its impact at the currently available energy range might still be noticeable, if very small. There are several reasons why these high-precision tests of the SM are challenging. One is the experimental uncertainties that are always present, albeit already impressively small. Another is the enormous amount of data produced at experiments like the LHC. In order to measure the most rare of processes, increasingly large numbers of events have to be processed to identify the relevant ones. Even if those signal events happened much more often, there would still be fundamental, physical constraints, like the fact that all neutrinos escape the detectors unnoticed and need to be reconstructed from missing transverse energy. Moreover, the particles that are registered in the detectors are only the decay products of the much heavier and very short-lived particles whose properties and interactions are the actual target of the experiment.

One of the most important tools used in particle physics to mitigate those challenges are simulations. Modern event generators like MadGraph5_aMC@NLO [5] or Sherpa [1] are capable of calculating the total and differential cross-sections of a given process, providing simulated scattering events and handling the particles' decay. Generators like Sherpa and Pythia [10] are also capable of handling the hadronic and electromagnetic showers that follow. When those simulated events are then processed by a detector simulation, they can be directly compared to the actual experimental data. This way, the model which served as the basis for the simulation can be thoroughly tested and the experimental output well understood.

One feature of the Monte Carlo event generators mentioned above is their ability to accommodate different theories as the basis for the calculation. This can be achieved by formulating a BSM theory in the language of the Universal FeynRules Output (UFO). These UFO models can then be imported into the different event generators, making a simulation of events based on BSM physics possible. While Sherpa has been able to incorporate UFO models for a while [11], most BSM simulations today are still performed using MadGraph. This thesis aims to validate BSM simulations in Sherpa, using two different UFO models applied to different physics processes. The main focus is the SMEFTsim model [3], which introduces dimension-six Effective Field Theory (EFT) operators into the SM Lagrangian. The model is applied to a same-sign W^+ Vector Boson Scattering process. In a second, shorter section, the HHVBF_UFO model [4] is used to alter the Higgs boson self-coupling in a process with a ssWWhjj signature.

The motivation for such validations is simple: In contrast to experimental data, simulated events are highly susceptible to errors and biases introduced by the physicists' understanding of the theory as well as its practical implementation. Being able to cross-check simulated results by performing the calculations independently with different pieces of software makes those mistakes less likely and provides the opportunity to study the impact of the simplifications and approximations employed in achieving those results. The more confidence there is in the predictions made by the simulations, the more useful they can be in the comparison to real data and the search for BSM physics. Hopefully, this thesis can be a part of establishing Sherpa as a viable option for BSM simulations in the future.

As the first step in this thesis, the necessary theoretical background is introduced. This includes an overview of the Standard Model of Particle Physics, with a focus on the Electroweak and Higgs sectors. The two relevant extensions of the Standard Model and the processes they are tested on are introduced. The theoretical background is followed by a section describing the LHC and ATLAS detector, as well as the necessary software tools. This leads to the results of the validation, first for the SMEFTsim model in the vector boson scattering process and then for altering of the Higgs self-coupling with the HHVBF_UFO model. Finally, the results are summarized and an outlook for future research is given.

2 Theoretical Background

2.1 The Standard Model of Particle Physics

The following section gives a very brief introduction to the SM. After introducing the symmetries that govern the interactions of the fundamental particles as well as the particles themselves, the emphasis is then laid on the electroweak sector of the SM and the basic principles of the Higgs mechanism.

2.1.1 Symmetries and Particle Content

The SM aims to describe three of the four observed fundamental interactions: the weak, strong and electromagnetic interactions. Gravity is not included, being instead described by Einstein's Theory of General Relativity [12]. The SM can be divided into two parts: Electroweak Theory, which unifies the electromagnetic and weak interactions, and Quantum Chromodynamics (QCD), which describes the strong interaction. Both of these are Yang-Mills theories, which means that the nature of the described interactions is determined by the theory's invariance under a set of local, non-abelian gauge transformations [13]. In the language of group theory, the gauge transformations of the electroweak sector form an $SU(2) \otimes U(1)$ gauge group. QCD, in turn, is invariant under transformations from an $SU(3)$ group. Overall, the symmetry group of the SM can be written as

$$SU(2)_L \otimes U(1)_Y \otimes SU(3) \qquad . \tag{2.1}$$

The Noether theorem [14] requires that in any case of invariance under a set of continuous transformations there must be a conserved current and related charge. In the case of the SM, the conserved charges in question are the particles' weak hypercharge and weak isospin, as well as their colour charge. A particle's electric charge is a linear combination of its weak hypercharge Y and the I_w^3 component of its weak isospin: $Q = I_w^3 + \frac{1}{2}Y$.

In order to achieve a theory for charged particles with local gauge invariance, the introduction of gauge fields is necessary. Those vector fields are associated with spin 1 vector particles called bosons, which can be understood as mediating the interactions. The gauge fields that are introduced in order to maintain the gauge invariance of the SM Lagrangian are then recombined in the process of electroweak symmetry breaking. All in all, the SM contains twelve gauge bosons. The photon mediates the electromagnetic interaction, while the two charged $W^{\pm}$ bosons and the electrically neutral Z boson characterize the weak interaction. The strong interaction is mediated by eight gluons (g), each of different colour charge.

While the Standard Model predicts the interactions between particles, it does not predict the number or nature of the particles involved. Instead, the particle content of the model is the result of experimental evidence. So far, there appear to be three generations of spin 1/2 particles, or fermions. The second and third generations are copies of the first one, except for a distinct difference in mass. There are two categories of fermions: leptons on the one hand, including electrons (e^-), muons (μ^-) and tauons (τ^-) as well as their corresponding neutrinos, and quarks on the other hand. Each one of the fermions also has a corresponding anti-particle, whose charges are reversed. Together with the gauge bosons introduced above, as well as the Higgs boson (h), which will be discussed in more detail later on, they make up all the known fundamental particles. The particles' masses and charges are summarized in table 2.1.

Table 2.1: The particle content of the Standard Model. The mass values are given as reported in [15].

	Fermions										Bosons				
	Leptons				Quarks							Vector		Higgs	
	e	μ	τ	$\nu_{e,\mu,\tau}$	u	d	s	c	b	t	$W^{\pm}$	Z	γ	g	h
m [GeV]	$0.5 \cdot 10^{-3}$	0.106	1.777	$< 0.8e^{-9}$	$2.16e^{-3}$	$4.67e^{-3}$	0.093	1.27	4.18	172.69	80.377	91.188	0	0	125.25
Q	-1	-1	-1	0	2/3	-1/3	-1/3	2/3	-1/3	2/3	± 1	0	0	0	0
I_W^3	-1/2	-1/2	-1/2	1/2	1/2	-1/2	-1/2	1/2	-1/2	1/2	± 1	0	0	0	-1/2
C	0	0	0	0	C	C	C	C	C	C	C	0	0	$C\bar{C}'$	0

2.1.2 Electroweak Theory

Since this thesis focuses almost exclusively on processes related to the electroweak interaction, this following description will focus on the fundamental mechanisms of the electroweak sector, and entirely omit the details of QCD.

The aforementioned symmetry group of the electroweak sector consists of two parts: a U(1) symmetry and a SU(2) symmetry. The first requires the introduction of a gauge field B_μ and the hypercharge Y. The second symmetry implies an invariance under $SU(2)$ local phase transformations and therefore the introduction of three gauge fields and their corresponding bosons called $W^{(1)}$, $W^{(2)}$ and $W^{(3)}$. The physical $W^{\pm}$ bosons of the SM are linear combinations of the $W^{(1)}$ and the $W^{(2)}$ boson:

$$W_\mu^\pm = \frac{1}{\sqrt{2}}(W_\mu^{(1)} \mp iW_\mu^{(2)}) \qquad . \tag{2.2}$$

Experiments show that the weak interaction violates parity [16]. Specifically, the charged bosons of the weak interaction only couple to left-handed (LH) particles and right-handed (RH) anti-particles, and not to RH particles or LH anti-particles. This is accommodated by placing LH particles and RH anti-particles into SU(2) doublets, whereas RH particles and LH anti-particles form SU(2) singlets, as for example for the electron fields:

$$\Psi(x) = \begin{pmatrix} \nu_e(x) \\ e^-(x) \end{pmatrix}_L \qquad \text{weak isospin doublet, and} \tag{2.3}$$

$$\Psi(x) = \begin{pmatrix} e^-(x) \end{pmatrix}_R \qquad \text{weak isospin singlet.} \tag{2.4}$$

Since the singlets are not affected by the SU(2) transformations, the corresponding particles/antiparticles do not couple to the charged bosons. The third, electrically neutral boson of the weak interaction, the Z boson, and the photon as the boson of the electromagnetic interaction are constructed from the remaining boson of the SU(2) symmetry $W^{(3)}$ and the U(1) boson B_μ:

$$Z_\mu = \frac{g_W W_\mu^{(3)} - g' B_\mu}{\sqrt{g_W^2 + g'^2}} = +B_\mu \cos\theta_w + W_\mu^{(3)} \sin\theta_w, \tag{2.5}$$

$$A_\mu = \frac{g' W_\mu^{(3)} + g_W B_\mu}{\sqrt{g_W^2 + g'^2}} = -B_\mu \sin\theta_w + W_\mu^{(3)} \cos\theta_w, \tag{2.6}$$

with the weak mixing angle θ_w and the coupling parameters g' and g_w. This angle also describes the relationship between those coupling parameters and the coupling of the electromagnetic interaction e:

$$e = g_w \sin\theta_w = g' \cos\theta_w \qquad . \tag{2.7}$$

2.1.3 Introducing Masses using the Higgs Mechanism

The gauge invariance of the SM Lagrangian is achieved through the introduction of gauge fields through the covariant derivative D_μ. The gauge bosons in the SM, as well as the fermions, are observed to be massive. According to Quantum Field Theory, the mass terms for vector fields V_μ and fermionic Dirac fields Ψ in the Lagrangian would be expected to have the structure

$$\mathcal{L}_{\text{mass, vector}} = -\frac{1}{2}m^2 V_\mu V^\mu \qquad \text{and} \qquad \mathcal{L}_{\text{mass, fermion}} = m\bar{\Psi}\Psi \qquad , \tag{2.8}$$

respectively. However, adding such terms would violate the desired gauge symmetry. The solution to the problem of the vector boson masses was first introduced by Brout, Englert and Higgs [17, 18] and is known as the BEH or Higgs mechanism.
Its core working principles are now first explained in a simpler case and then transferred to the more intricate case of the SM. This general structure, as well as the concrete notation in this section follow the description in reference [19]. An alternative introduction can be found in reference [13].
In the simplified scenario, a complex scalar field $\Phi = \frac{1}{\sqrt{2}}(\Phi_1 + i\Phi_2)$ with the potential

$$V = \mu^2\Phi^2 + \lambda\Phi^4 \text{with} \quad \lambda > 0 \tag{2.9}$$

is considered. The corresponding Lagrangian

$$\mathcal{L} = -\frac{1}{4}F^{\mu\nu}F_{\mu\nu} + (D_\mu\Phi)^*(D^\mu\Phi) - \mu^2\Phi^2 - \lambda\Phi^4 \tag{2.10}$$

is invariant under the simultaneous U(1) local gauge transformation of both B_μ and Φ:

$$\Phi(x) \rightarrow \Phi'(x) = e^{ig\chi(x)}\Phi(x) \tag{2.11}$$

$$B_\mu \rightarrow B'_\mu = B_\mu - \partial_\mu\chi(x) \qquad . \tag{2.12}$$

In the case of a potential with $\mu^2 < 0$, there exists an infinite set of minima at $\Phi_1^2 + \Phi_2^2 = \frac{-\mu^2}{\lambda} = v^2$. These vacuum states do not share the and Lagrangian's invariance under the local gauge transformations. That is why choosing one of the possible minima is known as spontaneous symmetry breaking. Picking the arbitrary direction along the real axis, it is possible to choose $\Phi_0 = \Phi_1 + i\Phi_2 = v$ with the vacuum expectation value v and to write Φ as an expansion around that minimum:

$$\Phi(x) = \frac{1}{\sqrt{2}}(v + \eta(x) + i\xi(x)) \tag{2.13}$$

with real scalar fields ξ and η. Plugging this version of Φ into the Lagrangian would result in mass terms for both the scalar field η and the gauge field B, but also a massless so-called Goldstone boson ξ. This non-physical field can be gauged away by utilizing one of the local gauge transformations to switch to the unitary gauge, in which Φ takes the form

$$\Phi(x) = \frac{1}{\sqrt{2}}(v + h(x)) \qquad , \tag{2.14}$$

where $\eta(x)$ has been renamed to $h(x)$. With this, the Lagrangian density in the unitary gauge becomes

$$\begin{aligned}\mathcal{L} = \frac{1}{2}(\partial_\mu h)(\partial^\mu h) - \lambda v^2 h^2 - \frac{1}{4}F_{\mu\nu}F^{\mu\nu} + \frac{1}{2}g^2 v^2 B_\mu B^\mu \\ + g^2 v B_\mu B^\mu h + \frac{1}{2}g^2 B_\mu B^\mu h^2 - \lambda v h^3 - \frac{1}{4}\lambda h^4 \qquad .\end{aligned} \tag{2.15}$$

This includes mass terms for the Higgs field h itself as well as the gauge field, but it no longer contains the Goldstone boson, whose degree of freedom has been absorbed into the longitudinal polarization mode of the (now massive) gauge boson. This means that the goal of introducing masses for the gauge bosons without spoiling the gauge invariance of the original Lagrangian has been accomplished.

In the next step, these working principles need to be applied to the actual case of the SM. The local gauge invariance of the electroweak sector of the SM can be expressed as the $U(1)_Y \otimes SU(2)_L$ group. Appropriately, the covariant derivative that is introduced into the Lagrangian to achieve this is also more complex:

$$D_\mu = \partial_\mu + ig_W \mathbf{T} \cdot \mathbf{W}_\mu + ig' \frac{Y}{2} B_\mu \qquad . \tag{2.16}$$

This includes the generators of the symmetries, namely the weak hypercharge Y for the U(1) and $\mathbf{T} = \frac{1}{2}\sigma$ for the $SU(2)_L$ symmetry, in which σ is the vector containing the Pauli spin matrices. The Higgs model introduced for the SM is an electroweak doublet, which includes two complex scalar fields in an electrically charged and a neutral component:

$$\Phi = \begin{pmatrix} \Phi^+ \\ \Phi^0 \end{pmatrix} = \frac{1}{\sqrt{2}} \begin{pmatrix} \Phi_1 + i\Phi_2 \\ \Phi_3 + i\Phi_4 \end{pmatrix} \qquad . \tag{2.17}$$

With the potential remaining the same as in the simpler example, the vacuum states for this Higgs field meet the criterion $\Phi^\dagger \Phi = \frac{-\mu^2}{2\lambda} = \frac{v^2}{2}$. As in the easier example, a specific minimum can be chosen and Φ is expressed as an expansion around that minimum. In unitary gauge, this results in

$$\Phi(x) = \frac{1}{\sqrt{2}} \begin{pmatrix} 0 \\ v + h(x) \end{pmatrix} \quad . \tag{2.18}$$

In analogy to the earlier example, the consequence of this is spontaneous symmetry breaking and the emergence of mass terms for the four gauge bosons:

$$\frac{1}{8} v^2 g_w^2 (W_\mu^{(1)} W^{\mu(2)} + W_\mu^{(1)} W^{\mu(2)}) \tag{2.19}$$

$$\frac{1}{8} v^2 (g_W W_\mu^{(3)} - g' B_\mu)(g_W W^{\mu(3)} - g' B^\mu) \tag{2.20}$$

The physical fields are mass eigenstates that diagonalize these terms, resulting in two massive, charged $W^\pm$ bosons, a massive and neutral Z boson and the massless photon. While the ground state Φ_0 does not have the full gauge invariance of the electroweak sector, it is invariant under the $U(1)$ symmetry of electromagnetism. Since this symmetry remains unbroken, the corresponding boson, the photon, remains massless.
As mentioned above, the introduction of fermion masses by hand would destroy the desired gauge invariance as well. This can also be avoided thanks to the Higgs mechanism. The expected mass term for fermions in equation 2.8 does not respect the symmetries because left- and right-handed states are treated differently in the weak interaction. The introduction of the Higgs field in the shape of an electroweak doublet means that terms like

$$g_f (\bar{L} \Phi R + \bar{R} \Phi^\dagger L) \tag{2.21}$$

can be introduced, which are gauge invariant. After spontaneously breaking the symmetry by picking the ground state in equation 2.18, the resulting mass term and the Higgs interaction for the electron look like

$$-\frac{g_e}{\sqrt{2}} v (\bar{e_L} e_R + \bar{e_R} e_L) - \frac{g_e}{\sqrt{2}} h (\bar{e_L} e_R + \bar{e_R} e_L) \quad , \tag{2.22}$$

with the Yukawa coupling g_e. According to the expected shape of the fermionic mass term, the relationship between the Yukawa coupling and the electron mass is therefore $g_e = \sqrt{2} \frac{m_e}{v}$.

2.2 Beyond the Standard Model of Particle Physics

As discussed in the introduction (section 1), the simulations performed in this thesis make use of models that go beyond the SM. The following section explains the two ways in which the SM will be altered and the processes that will be used to validate those BSM samples.

2.2.1 Effective Field Theories in Vector Boson Scattering

Effective Field Theories

The SM has been very well tested within the confines of the experimentally accessible energy range. One possible kind of extension that is harder to test is new physics at very high energy scales, like the inclusion of new, very heavy particles for example. The SM Effective Field Theory (SMEFT) approach relies on the idea that while the new physics might be happening at a characteristic energy scale Λ which is much higher than the experimentally accessible energy range, it still causes small deviations from the SM at the available energy scale. The EFT aims to parametrize those effects through a systematic expansion of the SM Lagrangian by adding new, higher order operators.
Those new operators are constructed from the SM fields, and they respect the symmetries discussed in chapter 2.1.1. Their effect is suppressed by powers of $\frac{1}{\Lambda}$, with the SMEFT cut-off energy Λ. Each of the operators is also scaled by an individual coefficient called a Wilson coefficient. With the new operators, the SM Lagrangian, which includes operators of dimension four, is extended to

$$\mathcal{L}_{\text{SMEFT}} = \mathcal{L}_{\text{SM}} + \frac{c^{(5)}}{\Lambda} Q^{(5)} + \frac{1}{\Lambda^2} \sum_i c_i^{(6)} Q^{(6)} + \ldots \qquad . \tag{2.23}$$

This includes the only constructable dimension-five operator, also called the Weinberg operator [20]. Since it is lepton- and baryon-number violating, it is often omitted. It is followed by the dimension-six operators. A commonly used basis for the dimension-six operators is the Warsaw basis, which identifies 59 independent operators when baryon number conservation is assumed [21]. In the interest of limiting the scope, this thesis only considers the Q_W operator, which is defined as

$$Q_W = \epsilon^{ijk} W_\mu^{i\nu} W_\nu^{j\rho} W_\rho^{k\mu} \qquad , \tag{2.24}$$

with its Wilson coefficient c_W. This operator was chosen because it directly effects the

triple and quartic gauge vertices [22].
The introduction of new operators into the Lagrangian results in different kinds of changes. Depending on the chosen operator(s), new vertices might be introduced that are not allowed in the SM. The new operators also alter the existing SM vertices, as well as potentially other parameters of the SM, like the masses of the gauge bosons. These shifts of the SM parameters are described in detail in reference [23]. The simulations in this thesis only include the replacement of one SM vertex per diagram with a new physics vertex.
These replacements lead to the addition of new Feynman diagrams that need to be taken into account when constructing the matrix element, which is necessary for the calculation of differential and total cross-sections.
The cross-section depends on the square of the absolute value of the matrix element, which in turn is the sum of the amplitudes represented by the individual diagrams. This means that the impact of the new diagrams can be split into different terms (adapted from [24]):

$$|\mathcal{A}_{SMEFT}| = |\mathcal{A}_{SM}|^2 + \frac{c_W}{\Lambda^2} 2\,\mathrm{Re}(\mathcal{A}_W \mathcal{A}_{SM}^*) + \frac{c_W^2}{\Lambda^4}|\mathcal{A}_W|^2 \tag{2.25}$$

Splitting up the contributions in this way is known as decomposition. The first term describes the pure SM contribution $\mathcal{A}_{SM}$. The second term represents the interference between SM and EFT diagrams and is often called the linear contribution. The last term consists of only EFT diagrams $\mathcal{A}_W$ and is known as the quadratic contribution.

Vector Boson Scattering

One of the applications for this EFT approach is to search for and parametrize slight deviations from the expected mechanism of electroweak symmetry breaking outlined above in section 2.1.3. This can be done using the process of Vector Boson Scattering (VBS). As the name suggests, the process itself is characterized by the scattering of two vector bosons. As shown in figure 2.1, this can happen either directly in a quartic vertex or through the exchange of a vector or Higgs boson.
Without the contribution of a Higgs boson like the one in the SM, the cross-section of the scattering of two longitudinal $W^{\pm}$ bosons would keep growing with increasing centre of mass energy, leading to a violation of unitarity. The introduction of a Higgs boson leads to additional diagrams, whose contributions restore unitarity [26]. These cancellations hint at the fact that the self-coupling of vector bosons is tightly related to the details of electroweak symmetry breaking, which makes the VBS process a good starting point

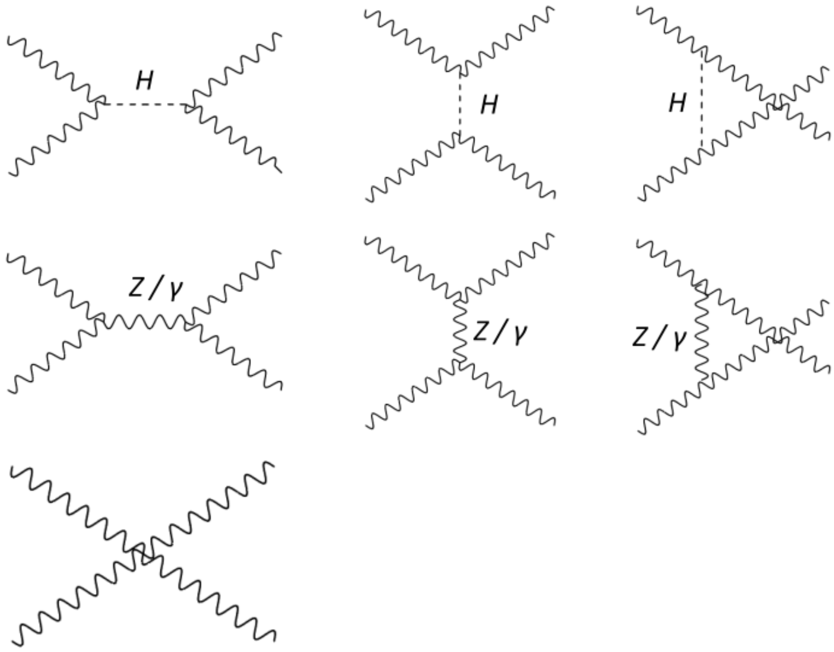

Figure 2.1: Core interactions for the process of vector boson scattering. Depending on the charge of the bosons involved, some diagrams have to be disregarded (adapted from [25]).

for physics beyond the SM.

In this thesis, the exemplary focus will be on the scattering of two same-sign W^+ bosons. This process has been observed at both ATLAS [27] and CMS [28]. At the LHC, the simplest way for the W^+ bosons to be produced is for them to be radiated off the quarks that formed the accelerated protons. In this particular case, the s-channel diagrams in figure 2.1 are not possible due to the conservation of electric charge.

The W^+ bosons then decay into stable particles. One of the possible decay channels consists of both of them decaying into a lepton and the corresponding neutrino. It is often selected, since the presence of the leptons makes the resulting final state more easily identifiable than the alternative hadronic decay. In addition to the leptons, the process is characterized by two jets, which are the detector signature of the hadronic showers caused by the final state's quarks. They are expected to have a high invariant mass and be well separated in rapidity [25].

The Feynman diagrams for the full process considered in this thesis can be found in figure 2.2. The figure includes both the actual VBS diagrams and three examples of diagrams that also have six electroweak couplings and contribute to the $e^+e^+\nu_e\nu_e jj$ final state, but which do not include any VBS. The initial state consists of two quarks and the final state is made up of two positrons, two electron-neutrinos and two quarks.

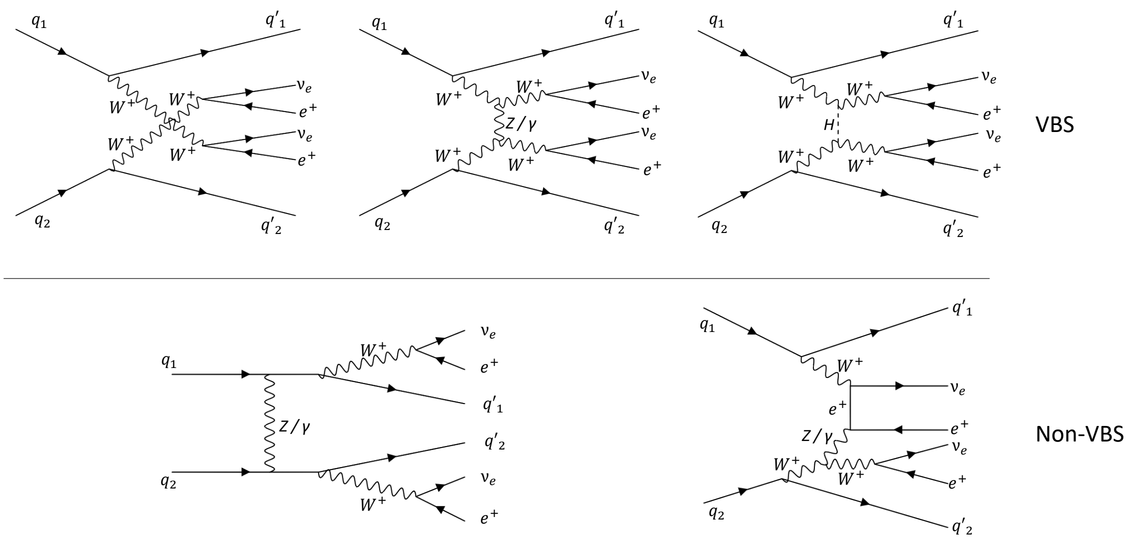

Figure 2.2: Selected Feynman diagrams contributing to the $e^+e^+\nu_e\nu_e jj$ final state. The first row shows all diagrams that are part of the vector boson scattering process, the second row shows two example diagrams with the same final state and perturbative order, that do not include vector boson scattering. Diagrams adapted from [29], p.5.

2.2.2 Modification of the Higgs self-coupling in the ssWWhjj signature

Another result of the structure of the Higgs sector outlined above is the Higgs boson self-couplings. While this is part of the SM prediction, it has not been observed so far. Measuring the Higgs self coupling would provide insight into important open questions, like the exact shape of the Higgs potential and the nature of the electroweak phase transition [30]. It also provides another opportunity to search for the small but potentially visible impact of unknown high energy physics in the experimentally accessible energy range [31]. One of the possible diagrams included in the process considered in this thesis is shown in figure 2.3. It includes a triple Higgs coupling, whose coupling strength can be altered using the HHVBF_UFO model [4].

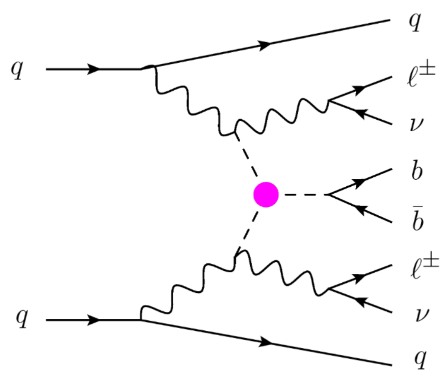

Figure 2.3: Feynman diagram of the process used to study the influence of an altered tri-Higgs coupling. Figure from [31], p. 2.

3 Experimental Setup and Software Tools

While all the events analysed in this work are the product of simulations, the eventual goal of all simulations is to compare the results to real experimental data. That means that it is still important to keep the characteristics, strengths and limitations of the experimental setup in mind. They dictate the choice of physical characteristics like the centre of mass energy of the collisions and inform the choice of variables when analysing the events.

3.1 The LHC

The Large Hadron Collider (LHC) is a particle accelerator located at the CERN (Conseil européen pour la Recherche nucléaire) particle physics laboratory close to Geneva. It was approved by the CERN council in December 1994 and utilizes the tunnel system and infrastructure originally built for its predecessor LEP (Large Electron-Positron Collider). LEP's operation was terminated in 2000 in order to make room for the new collider [32]. The following short description of the original design elements of the LHC are based on [33].
The 16.7 km long tunnel runs along a slightly tilted plane, resulting in a depth between 45 m and 170 m under the surface. While the LHC can be used to accelerate both protons and heavy ions, it is mostly used for proton-proton collisions. The CERN accelerator system serves as an injector chain for the LHC, as it did for LEP as well (Proton Synchrotron Booster (PSB) — Proton Synchrotron (PS) — Super Proton Synchrotron (SPS)).
The two proton beams counter-rotate in separate rings and are brought to collision at four interaction points. Two of them are the location of the two general purpose high luminosity experiments, ATLAS and CMS. The other two interaction points are at the ALICE detector, which is specialized for heavy ion collisions, and LHCb, which specific-

ally aims to study b quarks. There are five additional, smaller experiments that utilize the collider: TOTEM and LHCf for protons in ATLAS' and CMS' forward directions, FASER for the search for light and very weakly interacting particles, MoEDAL-MAPP for the search for magnetic monopoles and SND@LHC for studying neutrinos. A schematic of the accelerator complex can be seen in figure 3.1.

The proton beams are guided around the beam pipes by a system of superconducting magnets which produce fields above 8 T. Their operating temperature is below 2 K, which is achieved through a superfluid helium cooling system.

The number of expected events per second N for any given process can be calculated using the cross-section of said process σ and the machine luminosity L: $N = L\sigma$. The original goal for the proton collisions included a luminosity of $L = 10^{34}\,\mathrm{cm}^{-2}\,\mathrm{s}^{-1}$ in the high-luminosity experiments ATLAS and CMS, as well as a bunch spacing of 25 ns at a centre of mass energy of 14 TeV.

In 2008, the first proton beam was successfully steered around the collider rings [34]. After a technical incident in 2008 caused by a faulty electrical connection [35], the first data taking period, often referred to as Run 1, began in 2009. The centre of mass energy of the proton collisions increased from 3.5 TeV to 4 TeV over the course of Run 1 [36]. It was followed by a shutdown period (LS1), in which the technology and infrastructure of the accelerator were serviced and updated [37]. This enabled the accelerator to run at a centre of mass energy of 13 TeV in the second data taking period from 2015 to 2018 [38] [39]. Run 2 was in turn followed by another long shutdown period from 2018 to 2023 (LS2). During this, the accelerator was upgraded again. This included preparations for the planned future of the LHC: the High Luminosity LHC [40]. As of now, the third period of data taking (Run 3) has begun, with the LHC now operating at a centre of mass energy of 13.6 TeV [41]. This run will be followed by another round of upgrades, with the start of the High Luminosity era of the LHC expected to begin in 2029 [42].

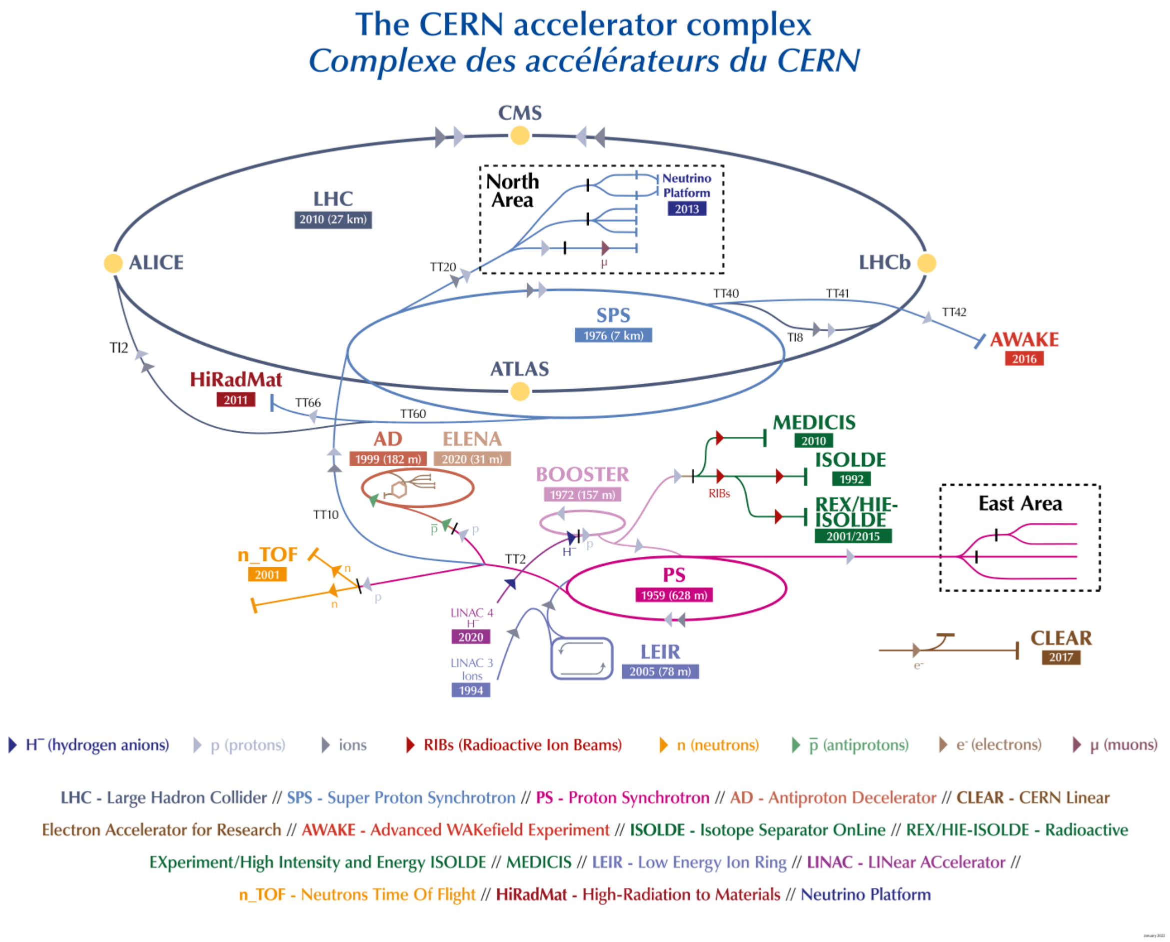

Figure 3.1: The accelerator complex at the CERN laboratory in Geneva [43].

3.2 The ATLAS Detector

The ATLAS detector is a high luminosity, general purpose detector with a generally cylindrical structure, at the center of which lies a collision point of the two LHC beams. A schematic depiction can be seen in figure 3.2. The following overview describing its main design features is a summary of [6]. The design addresses many challenges inherent in the detection of high-energy collision events. The enormous number of collisions combined with the large amount of radiation require electronics as well as detection elements that are both very fast and radiation hard. In addition to that, in order to avoid any particle tracks or energy deposits not being recorded, the detector coverage needs to extend as close to the beam line as possible and space taken up by infrastructure like electrical wiring needs to be minimized.
The detector has a forward-backward symmetry with respect to the interaction point. Many of its systems are divided into a barrel section parallel to the beam line and end-cap regions, which are perpendicular to it. In order to process billions of collisions a second, a trigger system reduces the amount of data that is recorded. It operates in several stages and uses some of the detector information to decide whether each event should be processed further or discarded [45].
The following description will first establish the coordinate system used within the ATLAS detector and then proceed to discuss the most important elements of the detector, starting with the interaction point at the centre and moving outward.

Coordinate System

The origin of the ATLAS detector's coordinate system is the interaction point of the two proton beams. The beam line is represented by the z-axis, with the positive x-axis pointing towards the centre of the accelerator ring and the positive y-axis pointing upwards. This defines the x-y-plane as the transverse plane and therefore important variables like the transversal momentum (p_T) of jets and particles, as well as the transverse energy (E_T). Missing transverse energy is an important tool to deduce the presence of neutrinos, which otherwise escape the detector unrecorded. The azimuthal angle Φ is measured around the beam axis and the polar angle θ is defined as the angle to the beam axis. The pseudo-rapidity η is defined as $\eta = -\ln \tan(\theta/2)$, and offers a convenient alternative to the polar angle. A particle heading upwards, perpendicular to the beam, would have a pseudorapidity of $\eta = 0$, while a particle moving parallel to the beam would have an infinite pseudorapidity. Using this, the distance between particles or jets with respect

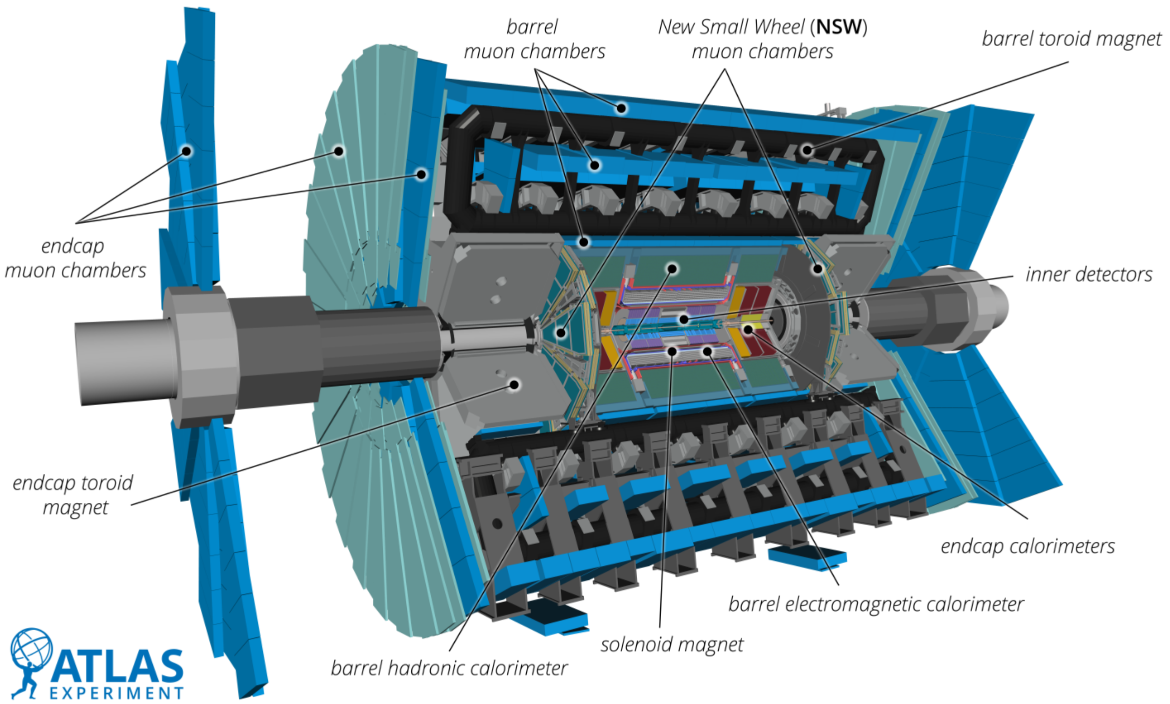

Figure 3.2: Schematic depiction of the ATLAS detector [44].

to pseudorapidity and azimuthal angle can be characterized with $\Delta R = \sqrt{\Delta\eta^2 + \Delta\Phi^2}$.

Inner Detector

The role of the inner detector is to record the tracks of charged particles as they travel towards the outer layers and to enable the measurement of both primary and secondary vertices. The innermost layer has the highest granularity, with 1744 silicon pixel sensors with 47232 pixels per sensor, resulting in 80.4 million readout channels. Each particle track crosses about three pixel layers. The pixel detectors are surrounded with four double layers of silicon microstrip trackers (SCT) with 6.3 million readout channels. Both the pixel detectors and the SCTs have an acceptance range of $|\eta| < 2.5$. The outer layer of the inner detector consists of Transition Radiation Trackers (TRT). The basic detection element of these are polyimide drift tubes with a diameter of 4 mm. The tubes are filled with a mixture of gases, namely xenon, carbon dioxide and oxygen. The TRTs provide 351,000 readout channels.
All the inner detector's components are arranged concentrically in the barrel region and in disks perpendicular to the beam in the end-cap regions. The entire Inner Detector is surrounded by a solenoid that fills it with a 2 T magnetic field, bending the tracks of

charged particles and enabling momentum and charge measurements.

Calorimeters

The Inner Detector is surrounded by the calorimeters, which record the energy deposited by electromagnetic and hadronic showers, respectively. They also prevent particles that are not muons or neutrinos from entering the surrounding muon system. The inner calorimeter is the electromagnetic one. It is a lead and liquid argon (LAr) detector with accordion-shaped kapton electrodes and consists of a barrel part ($|\eta| < 1.475$) and two end-cap parts ($1.375 < |\eta| < 3.2$). Outside of the electromagnetic calorimeter is the hadronic calorimeter. It consists of three parts: Directly surrounding the electromagnetic calorimeter is the hadronic tile calorimeter. It is a sampling calorimeter in which steel acts as the absorbing material and scintillating tiles serves as the active material. The other two components are the LAr hadronic calorimeter in the end-cap, consisting of copper plates interleaved with LAr-filled gaps, and the LAr forward calorimeter, which is integrated into the end-cap cryostats. This last component is itself divided into a copper-based part aimed at electromagnetic measurements and two tungsten-based components directed at hadronic measurements. All three of them are based on electrodes in the form of rods surrounded by tubes, with liquid argon as the active medium filling the gap between the two.

Muon Spectrometer

The muon calorimeter aims to measure the momentum of muons, which pass through all the inner layers of the detector without being stopped due to their high mass. Similar to the inner detector, the measurement of the particles' momentum is based on the bending of their tracks in a magnetic field. In this case, the magnetic field is provided by a large barrel torroid and two smaller end-cap magnets. The tracks themselves are recorded by tracking Monitored Drift Tube (MDT) chambers arranged in three cylindrical layers in the barrel region and three planes in the end-cap region. In the forward region ($2 < |\eta| < 2.7$) they are supplemented by Cathode Strip Chambers, which provide higher rate capability and a better time resolution.

3.3 Software Tools

Two Monte Carlo Event Generators were used in this work. The main focus is on the Sherpa software [1]. The version used in this thesis is equivalent to the state Sherpa's master branch as of November 28th 2023. The benchmark software that Sherpa will be compared to is the MadGraph5_aMC@NLO (MadGraph) event generator [5]. The Madgraph version used in this thesis is 3.4.2.
There are a couple of relevant differences between the two event generators. While Sherpa can be used for the production of both weighted and unweighted events, all events produced by MadGraph are unweighted. Sherpa is able to simulate not only the hard scattering process but also the electromagnetic and hadronic showers that occur afterwards. MadGraph however can not include the showers in its simulation. This means that MadGraph events are often subsequently processed with additional software like Pythia [10], which add the simulation of the showers. In the interest of reducing both the scope of this project and the number of steps in the workflow, the events for this technical validation were not showered. The events produced by MadGraph were fed directly into the Rivet analysis and not processed any further, and all elements of the shower simulations in Sherpa were turned off using the following settings:

- `FRAGMENTATION: None`
- `MI_HANDLER: None`
- `SHOWER_GENERATOR: None`
- `SHOWER_GENERATOR: None`
- `YFS: {MODE: None}`
- `ME_QED: {ENABLED: false}`
- `BEAM_REMNANTS: false`

In order to enable the alteration of the underlying physics model in both Sherpa and MadGraph, models formulated in the Universal FeynRules Output (UFO) [2] format are used. In Sherpa, these models can be included by running the included Sherpa-generate-model script, which generates the necessary source code. Sherpa includes two different matrix-element generators: the original AMEGIC++ and the newer Comix, but the usage of UFO models is only possible with Comix. In MadGraph the desired model has

to be placed in the program's `models` directory and can then be imported in the first stage of the event generation.
As mentioned before, this work utilizes two UFO models: SMEFTsim [3] for the inclusion of dimension-six operators in a VBS process, and HHVBF_UFO [4] for the alteration of the triple-higgs coupling strength. Most UFO models are available in the FeynRules model database [46], but unfortunately the versions of the two models used here relied on Python 2, which is incompatible with Sherpa's `Sherpa-generate-model` script. That is why the models used in this work were sourced from an ATLAS internal collection of models that have been updated to Python 3. The SMEFTsim version is 3.0.2, with the `Mw` input scheme and the topU3l flavour symmetry. The HHVBF_UFO is used with the `5fs` flavour scheme.
The generated events are analysed using the Rivet analysis framework [47]. The version used here is 3.1.7. It enables users to use both official analyses that are delivered as part of the software, and custom-built analyses. The analyses used for the SMEFTsim and HHVBF_UFO validations are discussed in the corresponding chapters.

4 Validation using the SMEFTsim Model

The first set of validation tests is performed with the SMEFTsim UFO model [3]. It allows the introduction of dimension-six EFT operators into the Lagrangian, as described in section 2.2.1. In this case, the operator Q_W and its Wilson coefficient c_w are used. In the EFT samples, c_w will be set to $c_w = 1$. Compared to current EFT limits of $c_w < 0.4$ [24] that is an unrealistically large value, but it was chosen in order to make the EFT contributions larger and therefore easier to compare.

4.1 Event Generation

4.1.1 Using interaction orders to enable decomposition

Both Sherpa and MadGraph give the user the ability to differentiate between the individual contributions of the decomposition approach described in section 2.2.1. This is achieved by utilizing a setting called interaction orders. They give the user the opportunity to control what Feynman diagrams and contributions should be included in the event generation. Even in simulations that are based purely on the SM these settings are commonly used to restrict the number of certain types of vertices. In the case of the process studied in this chapter they can be used to exclude any diagrams involving QCD vertices for example.
For the SMEFTsim model, the way to use interaction orders to target specific contributions is well documented in reference [48]. The first element of this project was to translate the documented MadGraph syntax into corresponding Sherpa syntax. Since the generation of individual EFT contributions is an important part of the intended validation, the following section outlines the syntax used in both Sherpa and MadGraph and why it selects the correct diagrams and contributions.
Both Sherpa and MadGraph offer interaction orders at two different levels. This work

will refer to them as the "amplitude" level (accessed via the `NP` syntax in MadGraph and the `Amplitude_Order` setting in Sherpa) and the "amplitude squared" level (`NP^2` in MadGraph and `Order` in Sherpa).
At the amplitude level, the interaction order decides what diagrams will be included in the calculation. Figure 4.1 shows a diagram that is part of the VBS process described in section 2.2.1. The diagram on the left includes only SM vertices. The vertex with two W^+ bosons and one Z boson can be altered by the introduction of the Q_W operator. In the diagram on the right, one of those has been replaced by this altered EFT vertex. Due to this new vertex factor, the amplitude of the diagram is now proportional to the new operator's Wilson coefficient c_W. The interaction order at the amplitude level expresses exactly that: Setting `NP = 1` in MadGraph syntax or `Amplitude_Order{NP:1, NPcW: 1}` in Sherpa selects only those diagrams that include exactly one EFT vertex and whose amplitudes are therefore proportional to c_W.
The setting at the amplitude squared level decides which terms are included when calculating the cross-section from the square of the absolute value of the matrix element. As already mentioned in 2.2.1, the EFT contributions can be separated like this:

$$\begin{aligned} |\mathcal{A}_{SMEFT}|^2 = |\mathcal{A}_{SM}|^2 \qquad & \sim c_W^0 \quad \text{(SM)} \\ +\frac{c_W}{\Lambda^2} 2\,\mathrm{Re}(\mathcal{A}_W \mathcal{A}_{SM}^*) \qquad & \sim c_W^1 \quad \text{(Linear)} \\ +\frac{c_W^2}{\Lambda^4} |\mathcal{A}_W|^2 \qquad & \sim c_W^2 \quad \text{(Quadratic)} \end{aligned} \tag{4.1}$$

In MadGraph an interaction order of one at amplitude squared level (`NP^2 == 1`) selects those terms from equation 4.1 that are proportional to c_W^1. Importantly, Sherpa defines this setting slightly differently. When using the interaction orders to limit the number of electroweak vertices for example, the `Order` setting does not refer to the exponent of e, but rather the exponent of $\alpha_{\text{EW}} = e^2/4\pi$. This means that while in MadGraph the linear contribution would be selected with `NP^2==1`, the same would be selected in Sherpa using `Order: {NP: 0.5, NPcW: 0.5}`.
Table 4.1 summarizes the resulting settings used for disentangling the individual EFT contributions in the simulations in this thesis. All process definitions also included the setting `QCD=0` or `Order/Amplitude_Order{QCD: 0}` to exclude any diagrams with QCD vertices. Since the UFO model SMEFTsim only operates at leading order, it is not necessary to restrict the number of electroweak couplings when using that model. In the case of a simulation using Sherpa's built-in SM, the number of electroweak vertices was set to six using `Order: {QCD: 0, EW: 6}`.

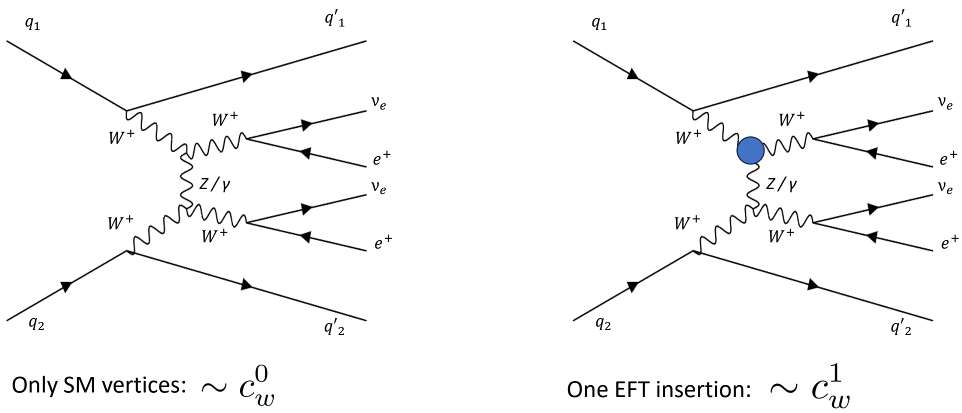

Figure 4.1: Two feynman diagrams with the same initial and final states. The left one includes only Standard Model vertices, in the right diagram one of them has been exchanged for a new-physics vertex.

Table 4.1: Interaction order settings used to achieve individual EFT contributions in the SMEFTsim model in MadGraph and Sherpa. The total contribution corresponds to the generation of a sample without decomposition.

	MadGraph	Sherpa
SM	`NP==0`	`Order {NP: 0, NPcW: 0}`
Linear	`NP<=1 NP^2==1`	`Max_Amplitude_Order: {NP: 1, NPcW: 1}, Order: {NP: 0.5, NPcW: 0.5}`
Quadratic	`NP==1`	`Amplitude_Order: {NP: 1, NPcW: 1}`
Total	`NP<=1`	`Max_Amplitude_Order: {NP: 1, NPcW: 1}`

4.1.2 General Settings

For the SMEFTsim validation, one million unweighted MadGraph and ten million weighted Sherpa events were produced for the SM, total and quadratic contributions. Since the linear term in the EFT decomposition can be negative, negative weights are possible for the events of the linear sample. That leads to comparibly large statistical uncertainties. In order to counteract this effect, the Sherpa events for the linear contribution were unweighted as well. This means that the linear samples consist of 200,000 unweighted Sherpa events and one million unweighted MadGraph events, respectively. The settings and variables used are summarized in table 4.2.

Table 4.2: Settings for the event generation in MadGraph and Sherpa using the SMEFTsim UFO model.

Variable	Value
Renormalization Scale	100 GeV
Beam Energy	6500 GeV
PDF Set	PDF4LHC21_40_pdfas
Generation Level Cuts	
Minimum Jet p_t	20 GeV
Minimum ΔR for jets	0.4
Maximum $\lvert\eta_j\rvert$	5
c_W	0 for SM, 1 for EFT contributions
All other Wilson coefficients	0
EFT cutoff energy Λ	1 TeV1 TeV
m_b	4.18 GeV
m_t	172.76 GeV
m_Z	91.1876 GeV
m_H	125.09 GeV
m_d,m_u,m_s,m_c, m_e, m_μ,m_τ	0
width Z	2.4952 GeV
width W	2.085 GeV
width top	1.33 GeV
width H	0.004 07 GeV
SM inputs for UFO (alpha s determined by pdf)	
m_W	80.387 GeV
G_f	$1.166\,378\,7 \times 10^{-5}\,\mathrm{GeV}^{-2}$
Sherpa Specific	
Process Definition	93 93 -> -11 -11 12 12 93 93
for regular SM: EW input scheme	Gmu
MadGraph Specific	
Process Definition	p p > e+ ve e+ ve j j

4.2 Rivet Analysis

The Rivet analysis used for all of the SMEFTsim validations is a slightly altered version of a pre-existing analysis named `MC_VBSCAN_MCComparison_withCR`, which was developed as part of the VBSCan COST action [49]. The changes mostly consist of disabling additional regions which are defined using more intricate cuts. They are not necessary for the validation intended here since there is no distinction between signal and background, and it is in the interest of the test to compare the respective contributions both in very populated areas of the histogram and the tails of the distributions.

The version of the analysis used here includes two phase spaces: There is one that includes all events that pass the very basic requirements for dressed leptons and acceptable jets, referred to as "No cuts", and one that includes a number of cuts aimed at the actual VBS process, referred to here as the "VBS phase space". The specific cuts used for both of them are listed in table 4.3.

The analysis first constructs a vector of dressed leptons out of the bare leptons of the final state by enforcing a clustering ΔR cone around each of them. It then constructs the jets using the anti-kt clustering algorithm. The jets are also required to have a minimum transverse momentum and a small enough $|\eta|$. At this point, the "No cuts" cross-section is determined. The events are then processed further to obtain the VBS phase space. Lepton p_t and $|\eta|$ cuts are enforced. If fewer than two leptons pass these cuts, the event is vetoed. Then the leading and sub-leading leptons (with the highest and second-highest p_t) are selected. They are required to have the same sign, since they are supposed to be the decay products of two same-sign W^+ bosons. The ΔR between any two leptons must be bigger than 0.3. After that, all jets which are too close to any of the leptons are removed. If after that cut there is fewer than 2 jets, the event is vetoed. Finally, the histograms are scaled using $\frac{\sigma}{\sum_i w_i}$, with the cross-section of the process σ and the sum of the weights w of all events.

The original analysis also reconstructs the kinematic properties of the W^+ bosons from their decay products, but that functionality is not utilized here.

Table 4.3: Phase space cuts in the Rivet analysis used for the SMEFTsim validation.

Phase Space	Cut	Value
Basic ("No cuts")	ΔR cone around dressed leptons	0.1
	Mimimum Jet p_t	30 GeV
	Maximum $\|\eta\|$ for leptons	4.4
VBS cuts	Minimum lepton p_t	20 GeV
	Maximum $\|\eta\|$ for leptons	2.5
	Minimum number of leptons	2
	Mimimum ΔR leptons	0.3
	Minimum ΔR jets/leptons	0.3
	Minimum number of jets	2

4.3 Sherpa-internal validation

The first step in validating the use of the UFO model in Sherpa is to make sure that it is consistent. In the first test, the SM limit of the UFO model is compared to the SM that is built-in in Sherpa. The following two tests validate the consistency of the decomposition approach by making sure that the sum of the individual contributions is equal to a sample without decomposition, and by reconstructing the linear and quadratic contributions from the total sample.

4.3.1 Comparing the Regular Sherpa SM to SM limit of UFO

In the case of SMEFTsim the SM limit entails setting all Wilson coefficients to zero and selecting the appropriate interaction orders (see section 4.1.1). All the settings listed in 4.2 are implemented for both generations. One of the necessary differences between the two samples is the input parameters for the SM. The UFO utilizes α_s, which in this case is determined by the Proton Density Function (PDF), the $W^{\pm}$ mass m_W and the Fermi constant G_F. The option closest to this in the regular SM in Sherpa is the `Gmu` input scheme, which utilizes the $W^{\pm}$ mass m_W, the Z mass m_Z, the Higgs boson mass m_H, their respective widths, and the Fermi constant G_F [50]. Apart from this one known difference, all settings can be realized in both Sherpa with and without the UFO model. The results of this comparison can be seen in figures 4.2, 4.3, 4.4 and 4.5. All uncertainties pictured are statistical uncertainties provided by the analysis.
The first comparisons in figure 4.2 show the integrated cross-sections for the sample representing the SM limit of the UFO and the sample for the regular Sherpa SM, before and after the VBS cuts. While the agreement is slightly better after the VBS cuts,

both agree within the uncertainties. While this is not the case for every single bin in the differential distributions shown in figures 4.3, 4.4 and 4.5, there appear to be no noticeable differences in shape between the two samples.

This good agreement lays a foundation for the following, more intricate comparisons.

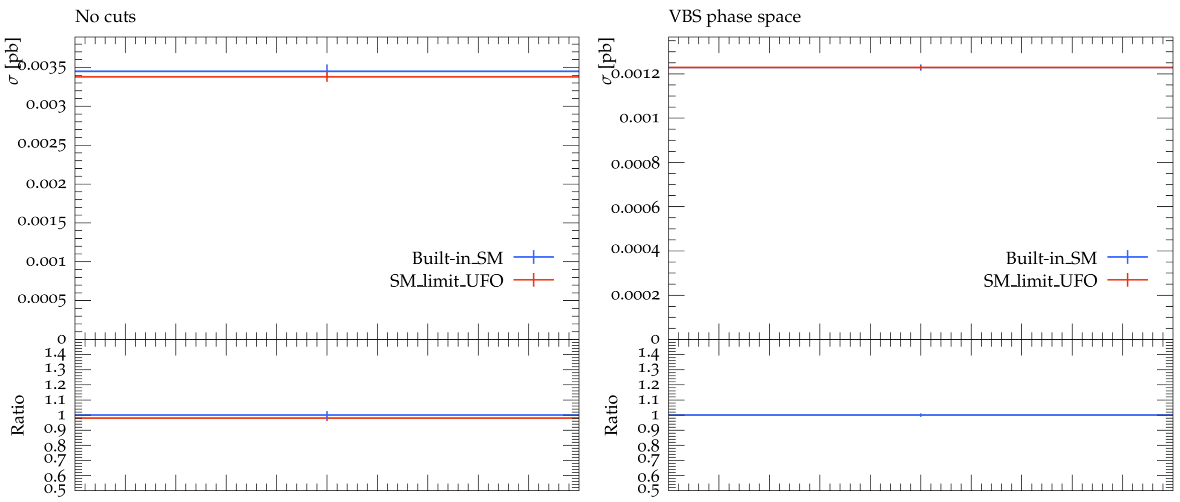

Figure 4.2: Total cross-sections of the samples generated with the UFO model's SM limit and Sherpa's built-in SM, before (left) and after (right) the VBS analysis cuts.

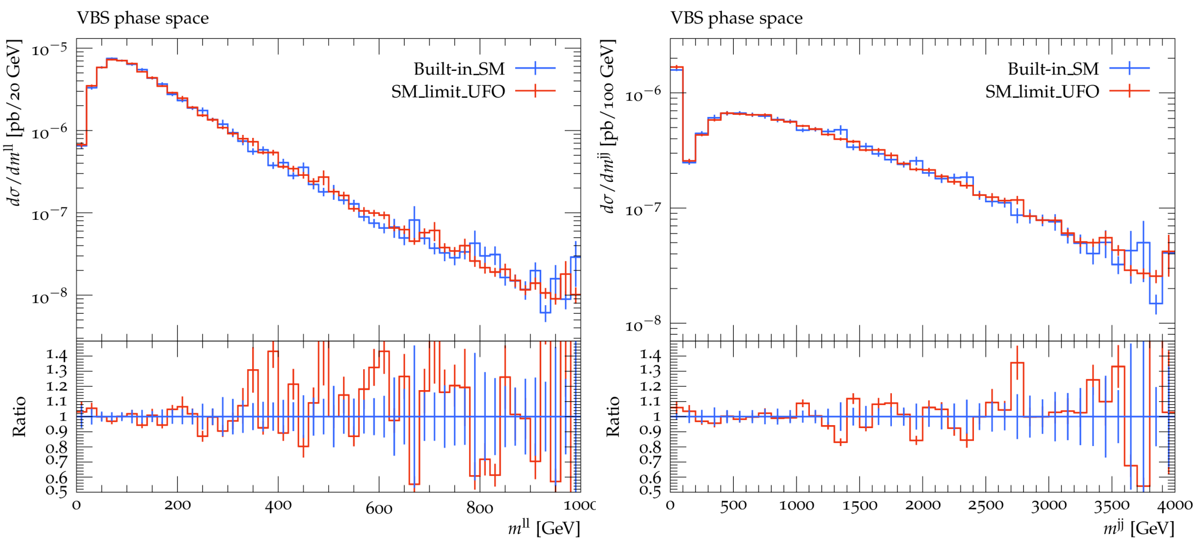

Figure 4.3: Comparison of the samples generated with the SMEFTsim model's SM limit and Sherpa's built-in SM. The histograms show the differential distributions of the invariant masses of the two leptons (left) and the two jets (right).

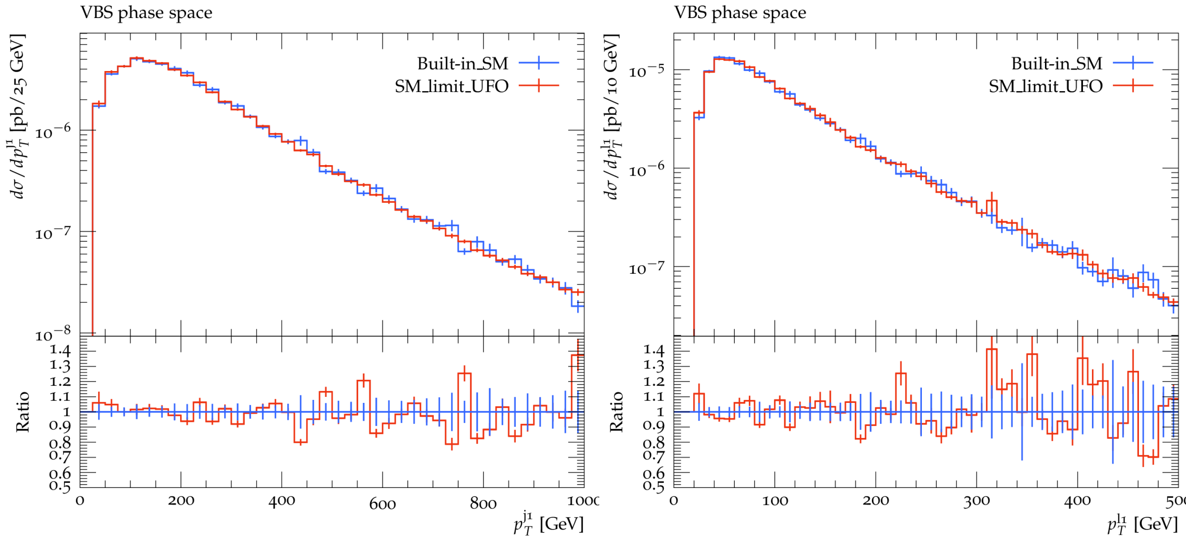

Figure 4.4: Comparison of the samples generated with the SMEFTsim model's SM limit and Sherpa's built-in SM. The histograms show the differential distributions of the transverse momenta of the leading jet (left) and the leading lepton (right).

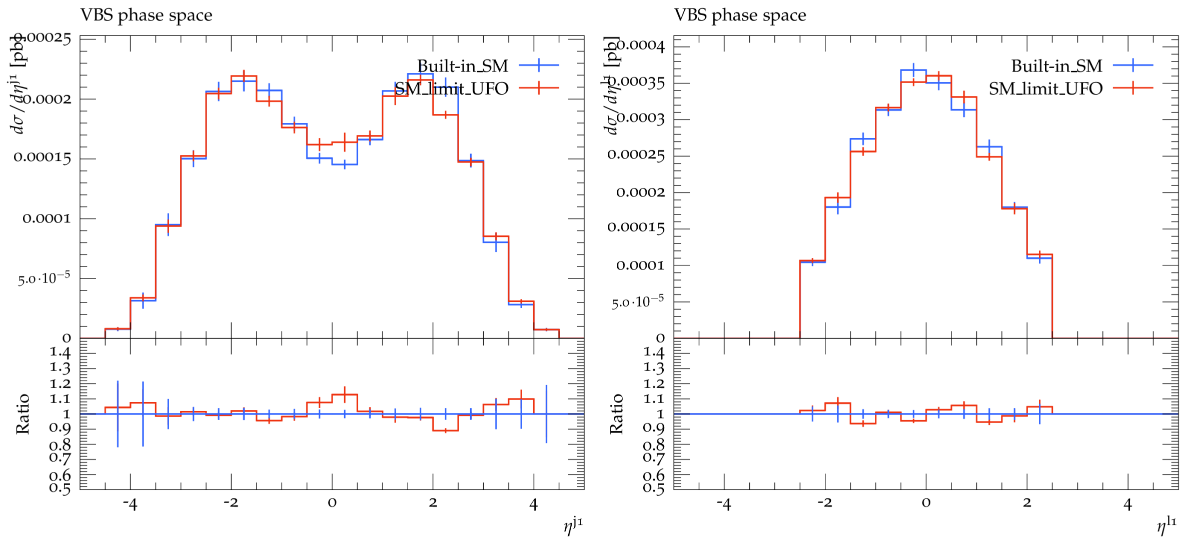

Figure 4.5: Comparison of the samples generated with the SMEFTsim model's SM limit and Sherpa's built-in SM. The histograms show the differential distributions of the pseudorapidity of the leading jet (left) and the leading lepton (right).

4.3.2 Stacking

One important feature of SMEFTsim is the possibility to discriminate between the different EFT contributions by using the interaction orders (as described in section 4.1.1). As equation 4.1 suggests, the sum of the SM, linear and quadratic contributions should be equal to the total sample, which represents the left side of the equation. This means that the decomposition process can be cross-checked by stacking the SM, linear and quadratic samples and comparing them to the total sample. Figures 4.6, 4.7, 4.8 and 4.9 show the results of that test. The areas shaded in red, blue and yellow represent the individual contributions and the black line shows the differential cross-section of the total sample. In other words: for the validation to be successful, the top of the stack of shaded areas needs to be meet the black line. In order to make the quality of the agreement more visible, the ratio plots show the sum of the individual contributions as a single purple line (referred to as "stack" in the legend).
The integrated cross-sections both before and after the VBS phase space cuts in figure 4.6 show very good agreement between the stack and the total sample. The same can be said for the differential distributions in figures 4.7, 4.8 and 4.9, which show agreement within the statistical uncertainties in almost all bins and no noticeable differences in shape.

4.3.3 Reconstructing Linear and Quadratic Contributions from the Total Sample

Another internal validation is the reconstruction of the linear and quadratic contributions from the total sample. This is achieved by generating total samples once with a positive value for the Wilson coefficient ($c_W = 1$) and then once again with the corresponding negative value ($c_W = -1$). From these samples, referred to in the following as $\texttt{TOT}^+$ and $\texttt{TOT}^-$, the linear and quadratic contributions with $c_W = 1$ ($\texttt{LIN}^+$ and $\texttt{QUAD}^+$) can be reconstructed:

$$\begin{aligned}
\frac{1}{2}(\texttt{TOT}^+ - \texttt{TOT}^-) = \frac{1}{2}((|\mathcal{A}_{SM}|^2 + \frac{1}{\Lambda^2}2\,\mathrm{Re}(\mathcal{A}_W\mathcal{A}_{SM}^*) + \frac{1}{\Lambda^4}|\mathcal{A}_W|^2)\\
-(|\mathcal{A}_{SM}|^2 - \frac{1}{\Lambda^2}2\,\mathrm{Re}(\mathcal{A}_W\mathcal{A}_{SM}^*) + \frac{1}{\Lambda^4}|\mathcal{A}_W|^2))\\
= \frac{1}{2}(\frac{2}{\Lambda^2}2\,\mathrm{Re}(\mathcal{A}_W\mathcal{A}_{SM}^*)) = \texttt{LIN}^+
\end{aligned} \tag{4.2}$$

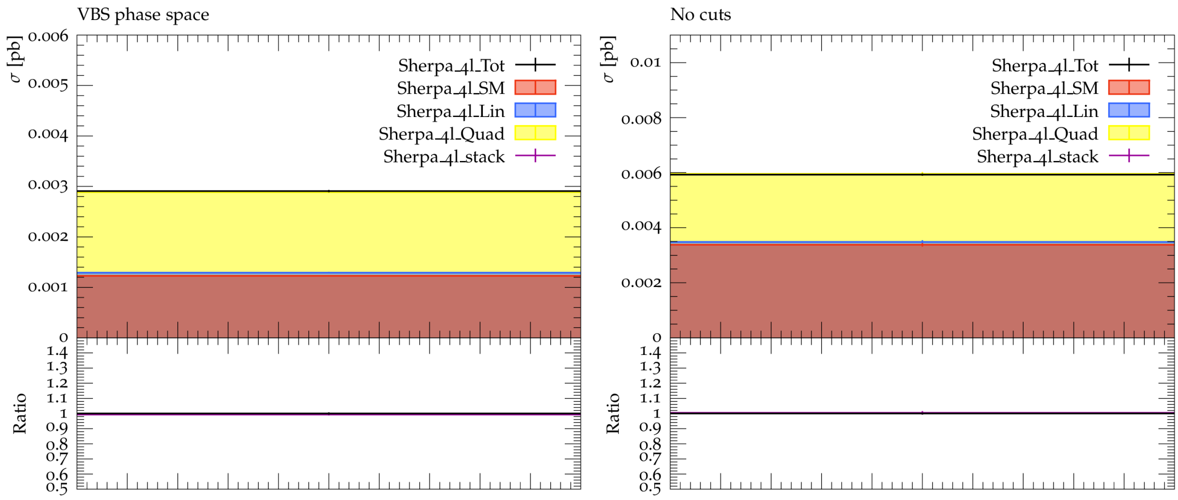

Figure 4.6: Comparison between the total sample produced without decomposition and the sum of the SM, linear and quadratic contributions. The purple line in the ratio plot labelled "stack" shows the sum of the individual contributions. The plots show the total cross-sections before (right) and after (left) the VBS analysis cuts.

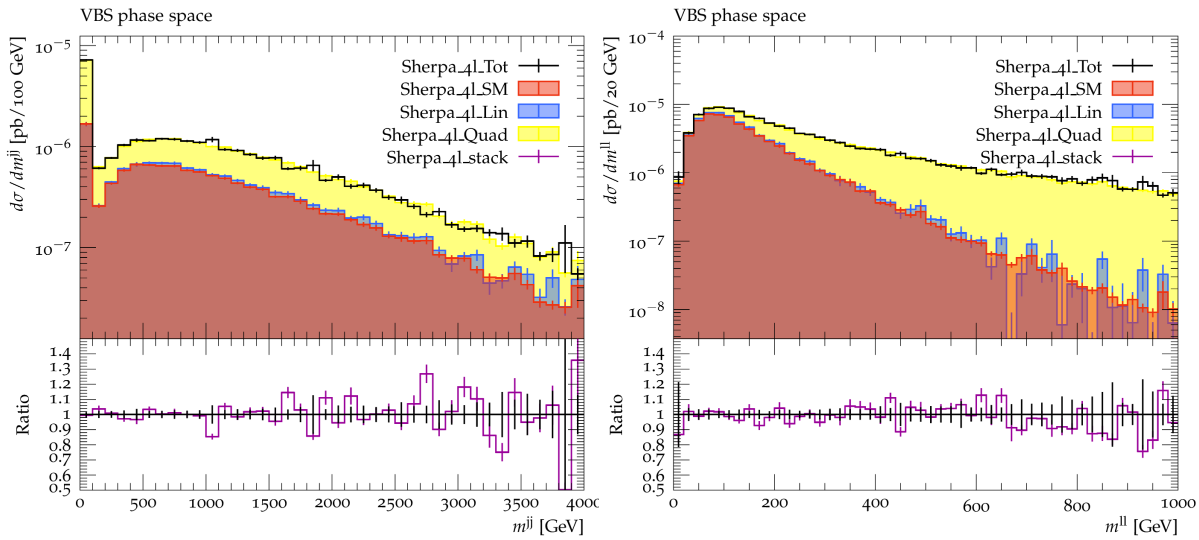

Figure 4.7: Comparison between the total sample produced without decomposition and the sum of the SM, linear and quadratic contributions. The purple line in the ratio plot labelled "stack" shows the sum of the individual contributions. The histograms show the differential distributions of the invariant masses of the two jets (left) and the two leptons (right).

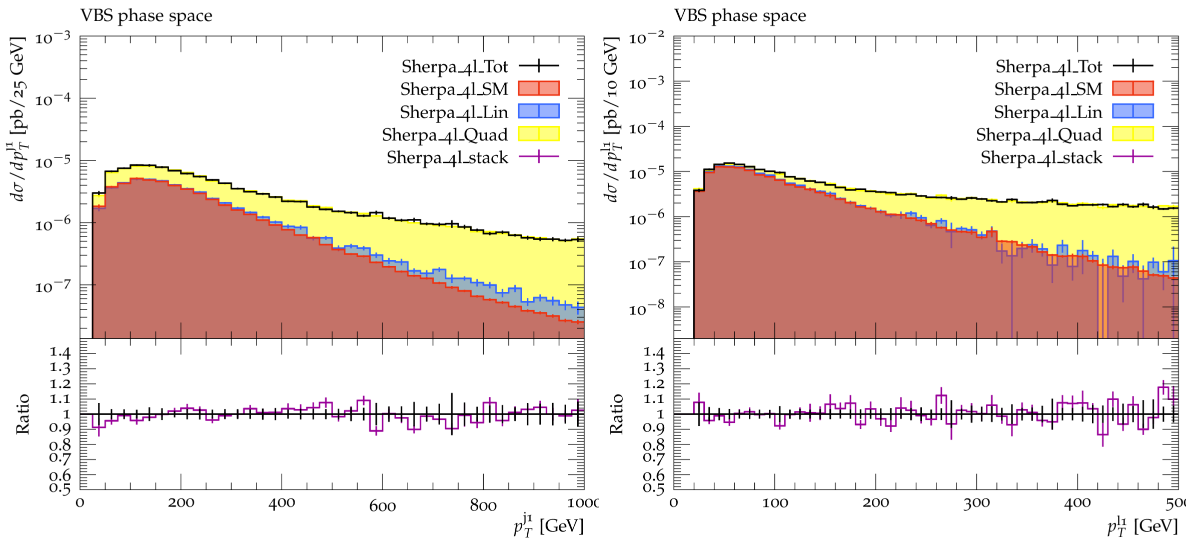

Figure 4.8: Comparison between the total sample produced without decomposition and the sum of the SM, linear and quadratic contributions. The purple line in the ratio plot labelled "stack" shows the sum of the individual contributions. The histograms show the differential distributions of the transverse momenta of the leading jet(left) and the leading lepton (right).

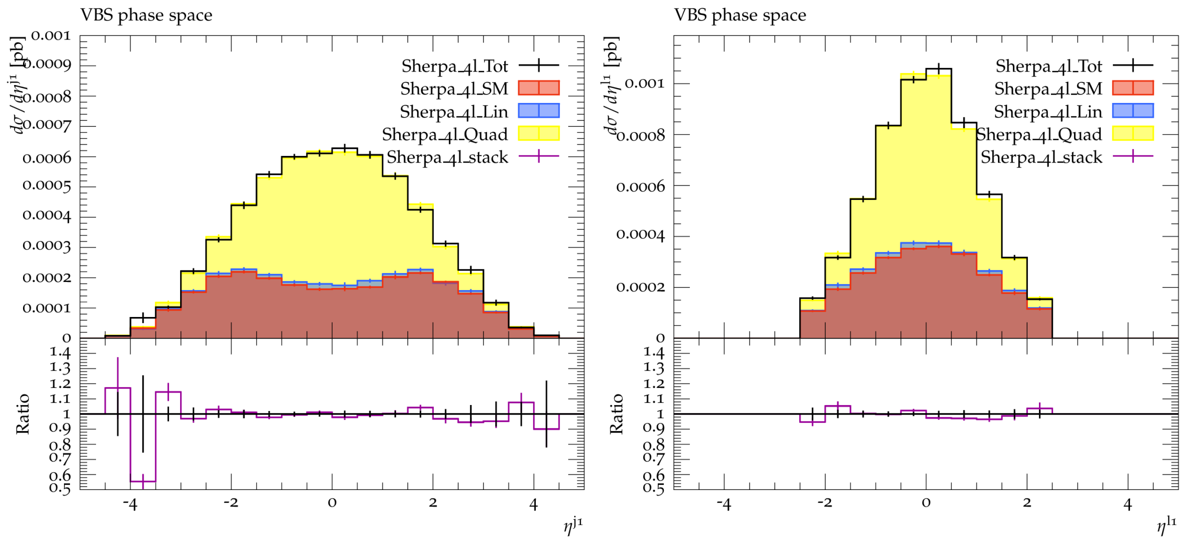

Figure 4.9: Comparison between the total sample produced without decomposition and the sum of the SM, linear and quadratic contributions. The purple line in the ratio plot labelled "stack" shows the sum of the individual contributions. The histograms show the differential distributions of the pseudorapidity of the leading jet (left) and the leading lepton (right).

$$\begin{aligned}
\frac{1}{2}(\texttt{TOT}^{+} + \texttt{TOT}^{-}) - \texttt{SM} = \frac{1}{2}((|\mathcal{A}_{SM}|^2 + \frac{1}{\Lambda^2}2\,\mathrm{Re}(\mathcal{A}_W\mathcal{A}_{SM}^*) + \frac{1}{\Lambda^4}|\mathcal{A}_W|^2) \\
+(|\mathcal{A}_{SM}|^2 - \frac{1}{\Lambda^2}2\,\mathrm{Re}(\mathcal{A}_W\mathcal{A}_{SM}^*) + \frac{1}{\Lambda^4}|\mathcal{A}_W|^2)) - |\mathcal{A}_{SM}|^2 \\
= \frac{1}{2}(2\cdot|\mathcal{A}_{SM}|^2 + 2\cdot\frac{1}{\Lambda^4}|\mathcal{A}_W|^2) - |\mathcal{A}_{SM}|^2 \\
= \frac{1}{\Lambda^4}|\mathcal{A}_W|^2 = \texttt{QUAD}^{+}
\end{aligned} \tag{4.3}$$

Comparing those reconstructed contributions to the individually generated ones constitutes another way of validating that Sherpa's use of the UFO model is consistent.

Figures 4.10 and 4.11 show that the results of this test for the linear contribution are not very conclusive. The reason for that are the very big statistical uncertainties in the reconstructed contribution. As equation 4.2 suggests, the reconstruction of the linear contribution is based on the subtraction of the $\texttt{TOT}^{+}$ and $\texttt{TOT}^{-}$ samples. Both of them have much larger cross-sections and therefore much larger absolute statistical uncertainties than the linear contribution. This means that the absolute uncertainty of their difference is very large compared to the actual linear contribution. The relative size of the linear contribution in comparison to the SM or quadratic contributions is a characteristic of this particular operator's effect on this specific VBS process. This particular test can be expected to be more conclusive in a combination of process and operator with a bigger linear contribution.

This expectation is supported by the fact that the corresponding test for the quadratic contribution is much more clear, as figures 4.12, 4.13, 4.14 and 4.15 show. The higher cross-section for the quadratic contribution means that the uncertainties are not as large in comparison, resulting in a much more conclusive comparison. Figure 4.12 shows that the agreement for the integrated cross-section after the VBS cuts is slightly better than without those cuts, but they both agree within the uncertainties. The differential distributions in figures 4.13, 4.14 and 4.15 also show agreement within the uncertainties between the reconstructed and the individually generated quadratic contributions.

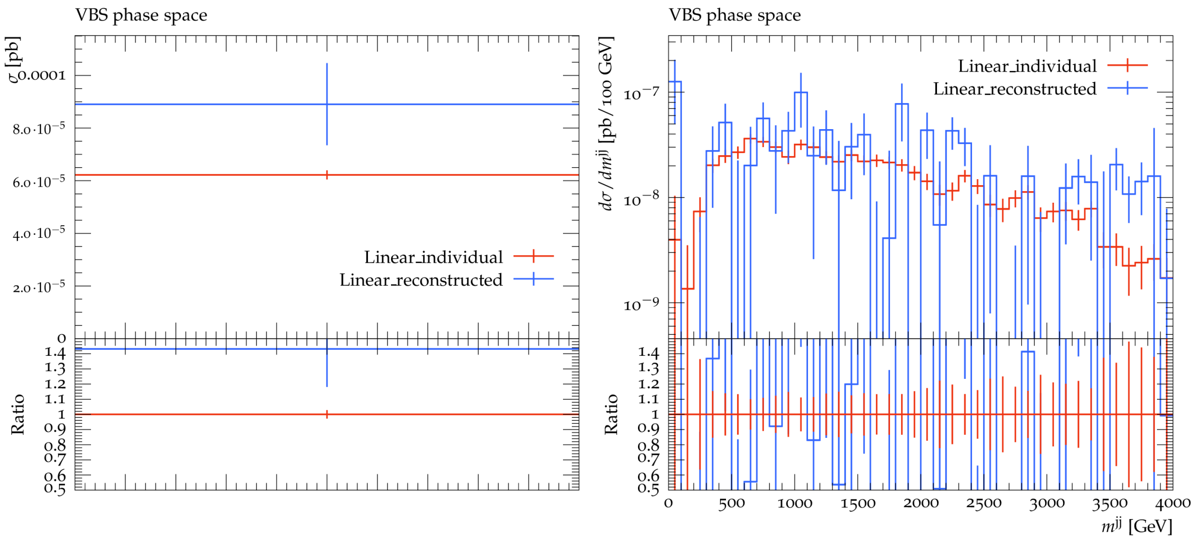

Figure 4.10: Comparison between the individually generated linear contribution and the linear contribution reconstructed from two total samples with opposite-sign Wilson coefficients. The plots show the total-cross section after the VBS analysis cuts (left) and the differential distribution of the invariant mass of the two jets (left).

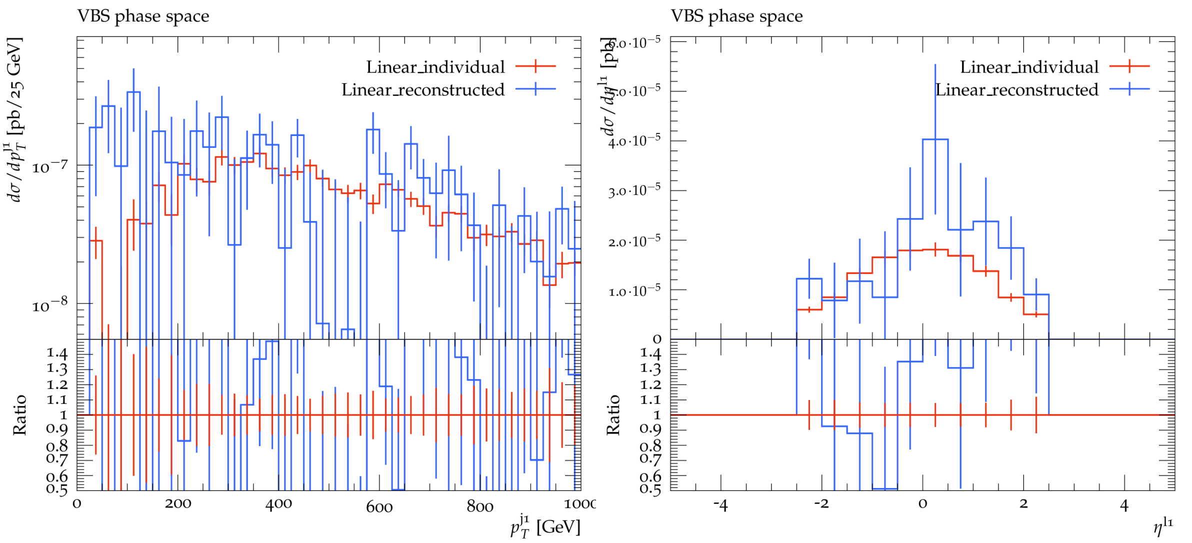

Figure 4.11: Comparison between the individually generated linear contribution and the linear contribution reconstructed from two total samples with opposite-sign Wilson coefficients. The histograms show the differential distributions for the transverse momentum of the leading jet (left) and the pseudorapidity of the leading lepton (right).

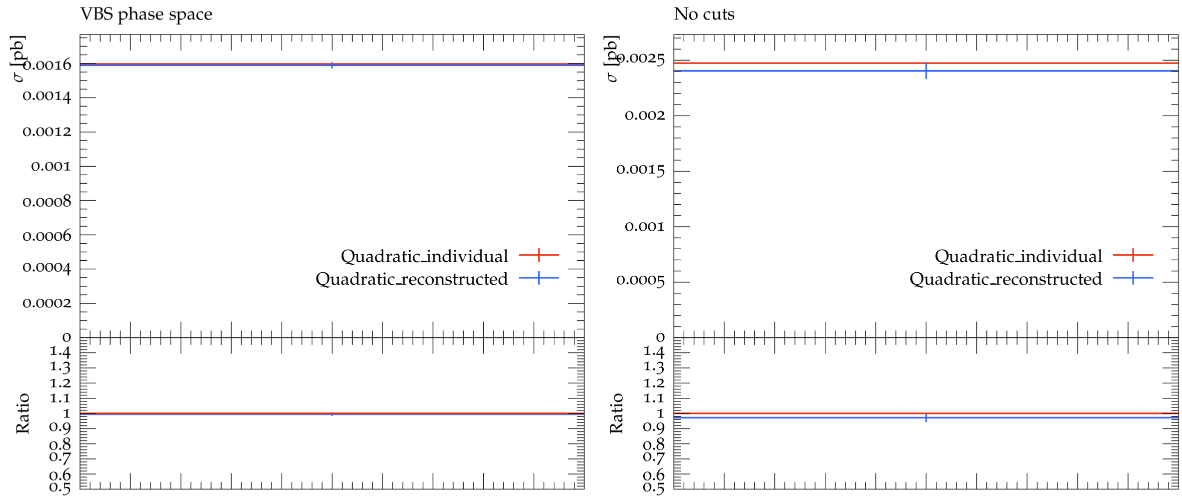

Figure 4.12: Comparison between the individually generated quadratic contribution and the quadratic contribution reconstructed from two total samples with opposite-sign Wilson coefficients and the SM contribution. The plots show the total cross-sections before (right) and after (left) VBS phase space cuts.

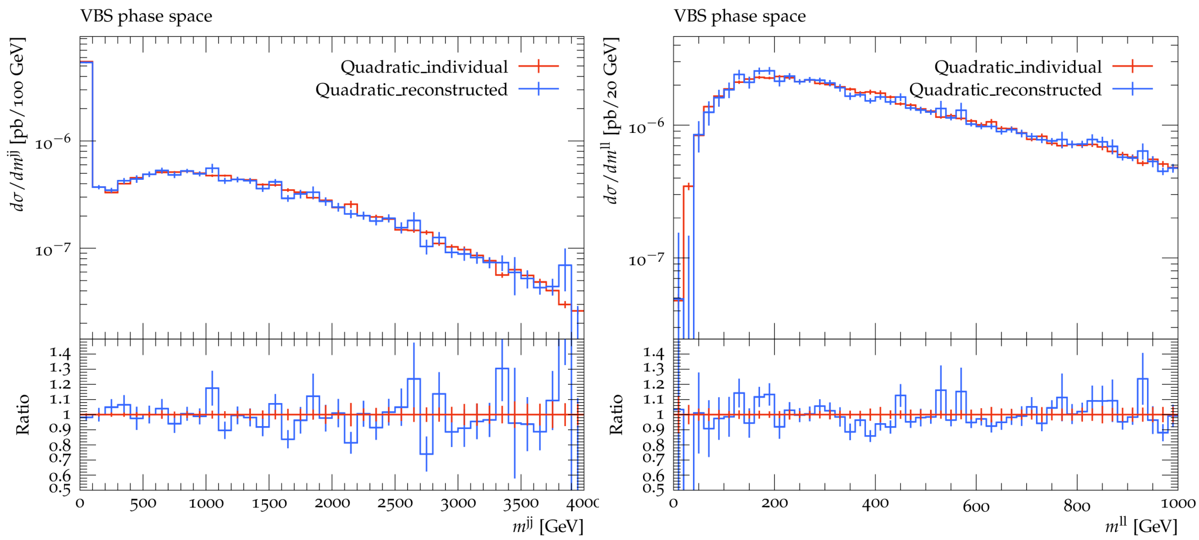

Figure 4.13: Comparison between the individually generated quadratic contribution and the quadratic contribution reconstructed from two total samples with opposite-sign Wilson coefficients and the SM contribution. The histograms show the differential distributions of the invariant masses of the two jets (left) and the two leptons (right).

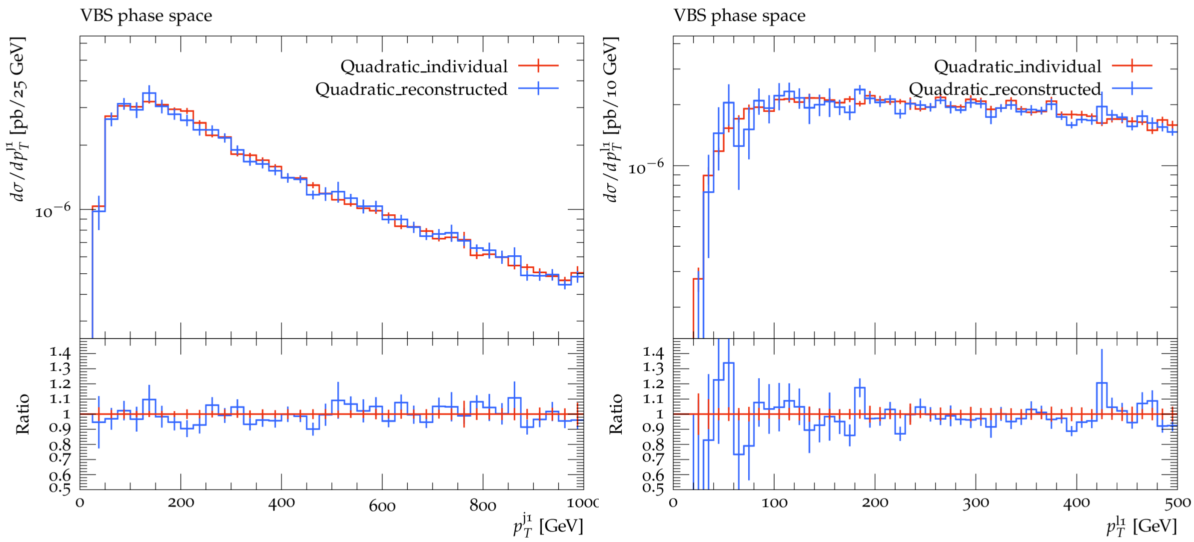

Figure 4.14: Comparison between the individually generated quadratic contribution and the quadratic contribution reconstructed from two total samples with opposite-sign Wilson coefficients and the SM contribution. The histograms show the differential distributions of the transverse momenta of the leading jet (left) and the leading lepton(right).

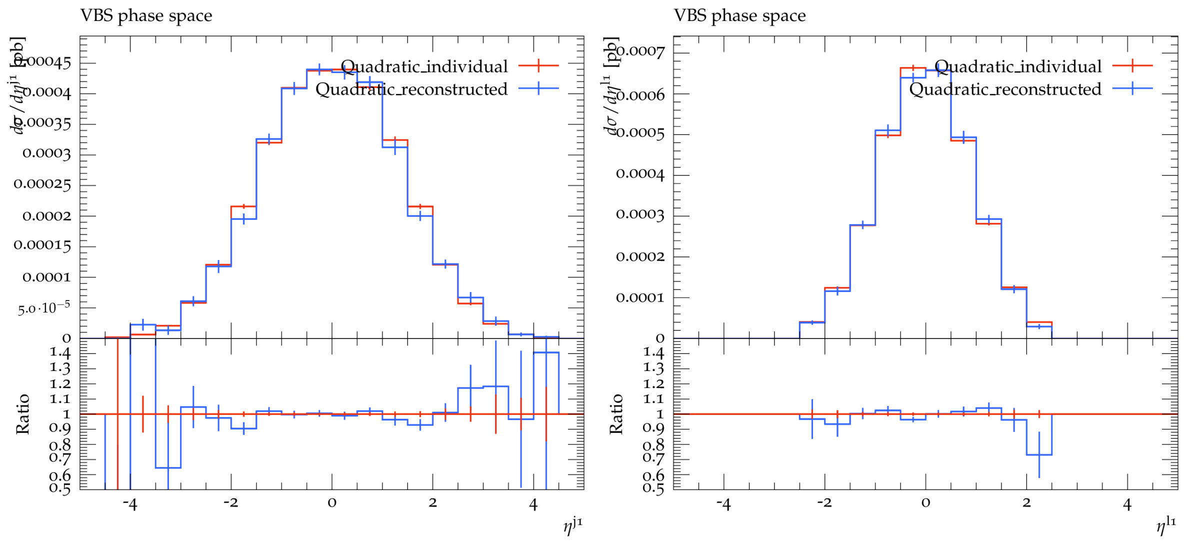

Figure 4.15: Comparison between the individually generated quadratic contribution and the quadratic contribution reconstructed from two total samples with opposite-sign Wilson coefficients and the SM contribution. The histograms show the differential distributions of the pseudorapidities of the leading jet (left) and the leading lepton(right).

4.4 Comparing MadGraph and Sherpa

Overall, the Sherpa-internal validations have shown that Sherpa's usage of the SMEFT-sim UFO model is consistent and that the decomposition behaves as expected. The next step is now to compare Sherpa's results to those of MadGraph, which is the more established tool for the creation of BSM events with UFO models.

4.4.1 SM contribution

Again, the first step is to ensure that the SM contributions agree with each other. Using two different software tools brings with it the challenge of translating syntax and settings from one program to the other. While the total cross-sections before and after the VBS cuts in figure 4.16 and the differential cross-sections of the invariant masses depicted in figure 4.17 and the pseudorapidities depicted in figure 4.20 suggest a good agreement between the UFO SM limit in Sherpa and MadGraph, figure 4.18 reveals that a systematic difference between the two samples remains. It shows a distinct shape difference between the transversal momenta of the leading and sub-leading jets $p_t^{\mathrm{j}1/2}$. While the difference is mostly visible in the ratio plot in the case of the leading jet, it is clearly visible even in the regular distribution for the sub-leading jet. As figure 4.19 shows, the problem is specific to the jets and does not appear in the case of the leading and sub-leading lepton.

The reason for this discrepancy could not be determined during the course of this project, but, as the following plots will show, the problem is exclusive to the SM contribution and does not appear for the linear or quadratic contributions. That suggests that it is likely to be caused by a user error, rather than a misinterpretation of the UFO model by Sherpa.

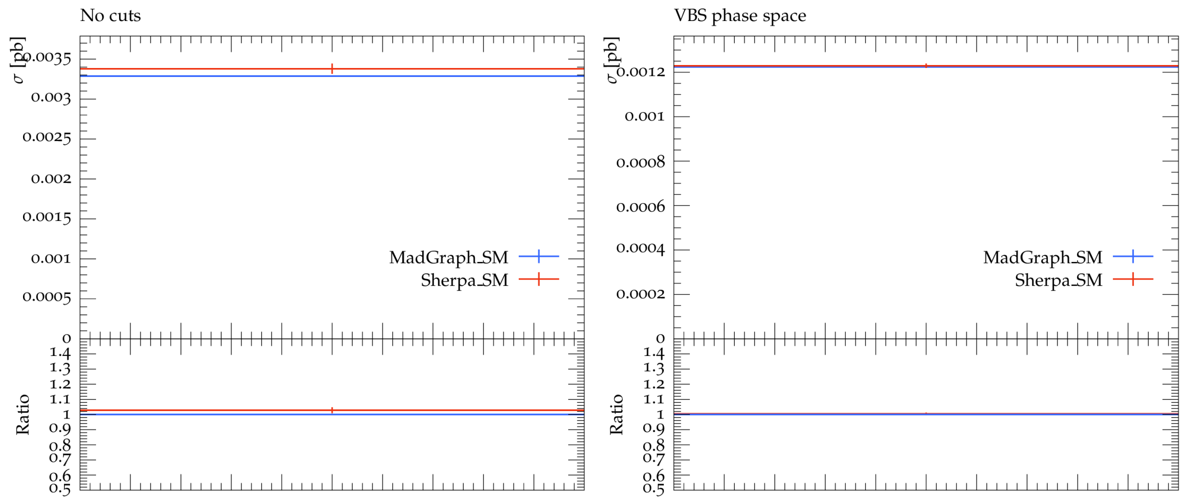

Figure 4.16: Comparison between the SM contributions produced with the SMEFT-sim model in MadGraph and Sherpa. The plots show the total cross-section before (left) and after (right) the VBS analyis cuts.

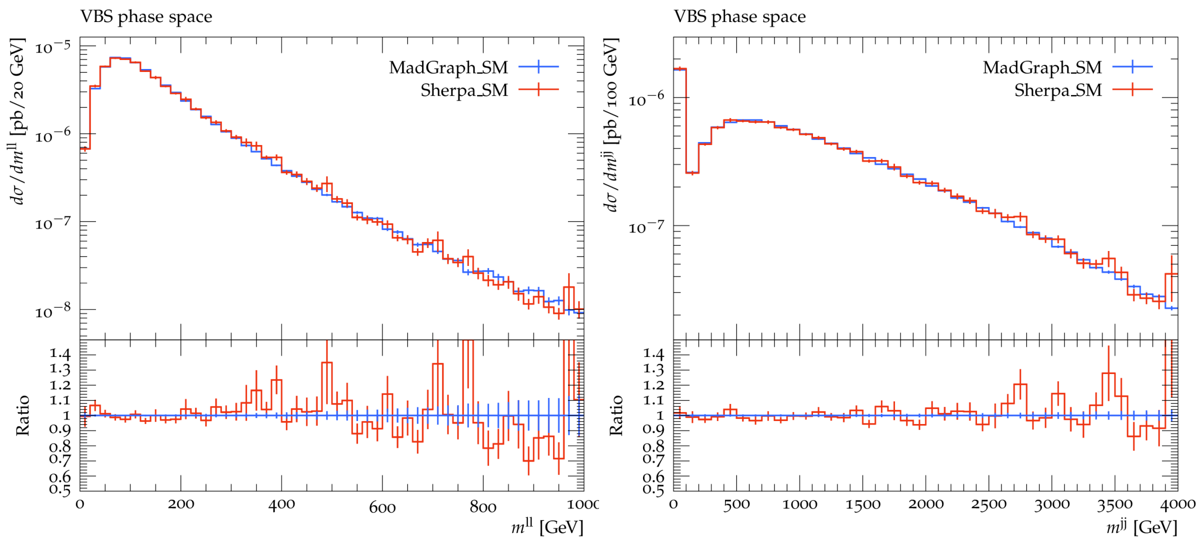

Figure 4.17: Comparison between the SM contributions produced with the SMEFT-sim model in MadGraph and Sherpa. The histograms show the differential distributions for the invariant masses of the two leptons (left) and the two jets (right).

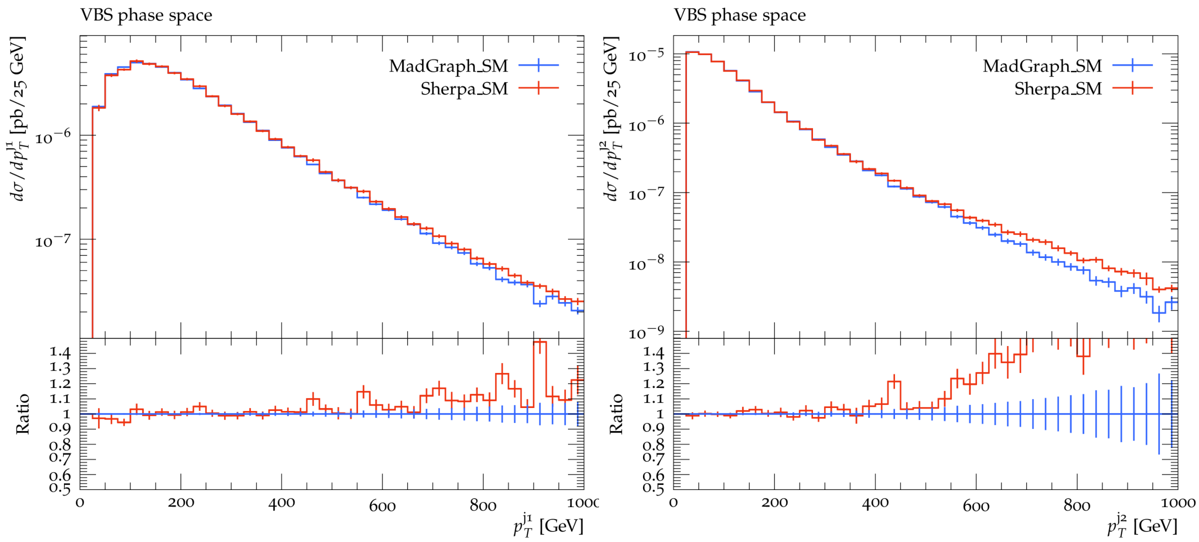

Figure 4.18: Comparison between the SM contributions produced with the SMEFTsim model in MadGraph and Sherpa. The histograms show the differential distributions for the transverse momenta of the leading (left) and subleading (right) jet.

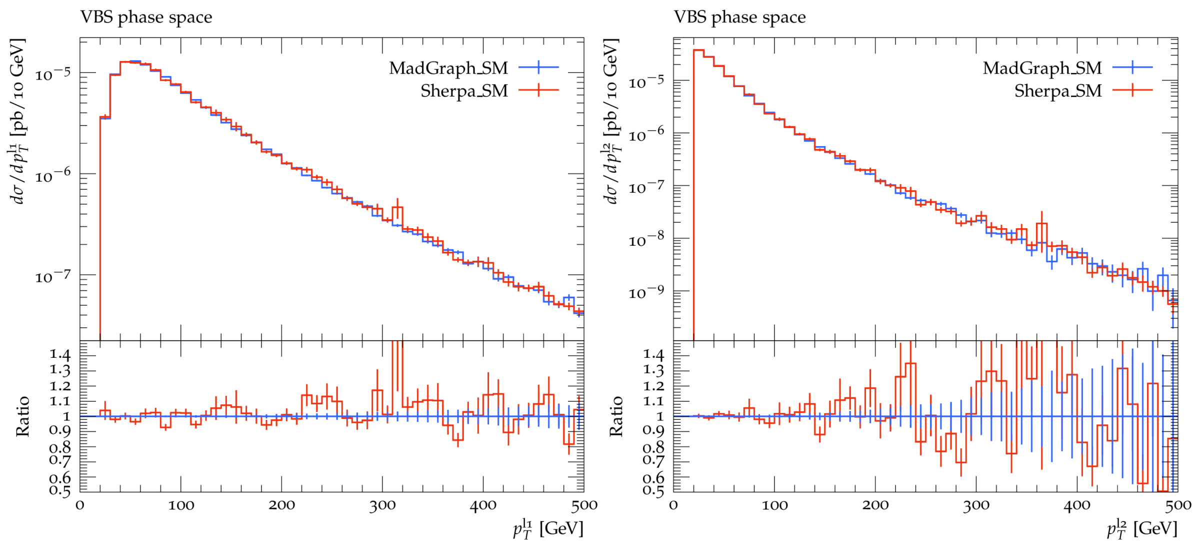

Figure 4.19: Comparison between the SM contributions produced with the SMEFTsim model in MadGraph and Sherpa. The histograms show the differential distributions for the transverse momenta of the leading (left) and subleading (right) lepton.

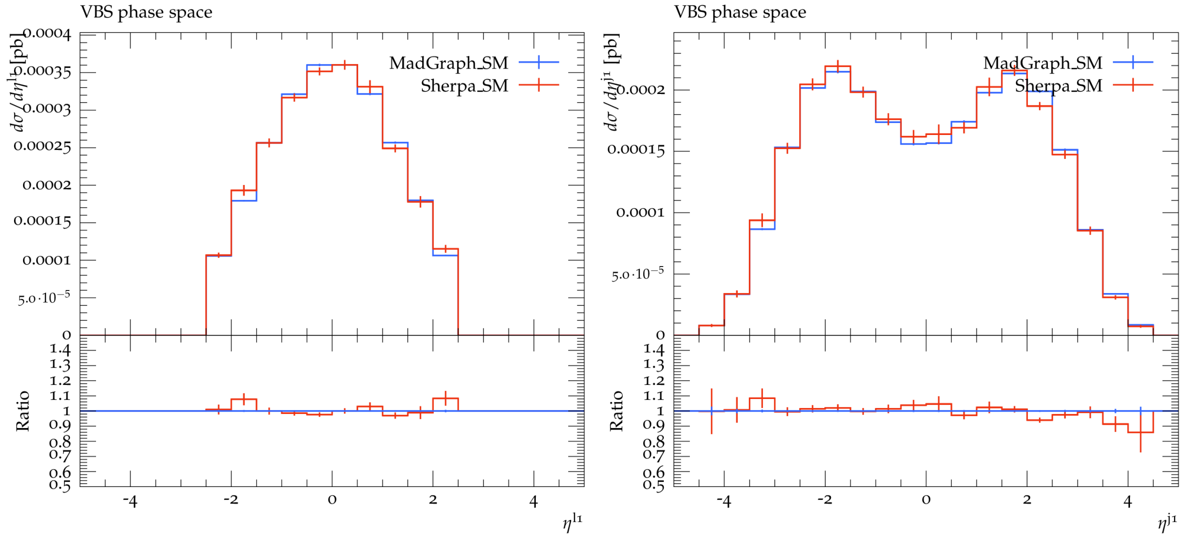

Figure 4.20: Comparison between the SM contributions produced with the SMEFT-sim model in MadGraph and Sherpa. The histograms show the differential distributions for the pseudorapidities of the leading lepton (left) and leading jet (right).

4.4.2 Linear and Quadratic Contributions

Once again the relatively large uncertainties of the linear sample make the comparison between MadGraph and Sherpa slightly less conclusive than the respective plots for the quadratic contribution. Nevertheless, figures 4.21 and 4.25 show that the integrated cross-sections before and after the VBS cuts for both the linear and quadratic contributions agree within their uncertainties. The differential distributions for the linear contribution in figures 4.22, 4.23 and 4.24 and for the quadratic contribution in figures 4.26, 4.27 and 4.28 also show good agreement. As mentioned before, figures 4.23 and 4.27 show that the discrepancy in the $p_t^{j1/2}$ does not appear in the EFT contributions.

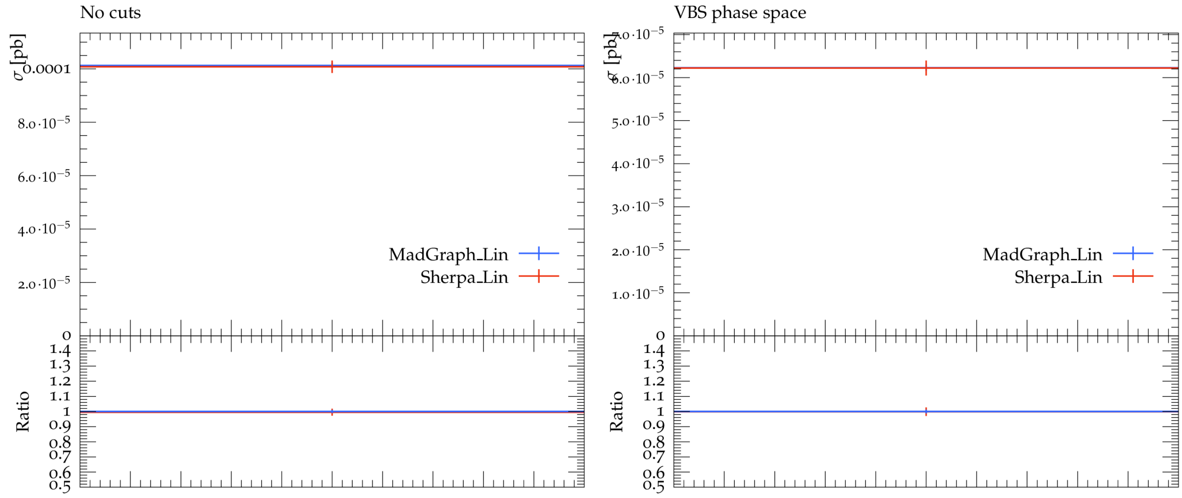

Figure 4.21: Comparison between the linear contributions produced with the SMEFTsim model in MadGraph and Sherpa. The plots show the total cross-section before (left) and after (right) the VBS analysis cuts.

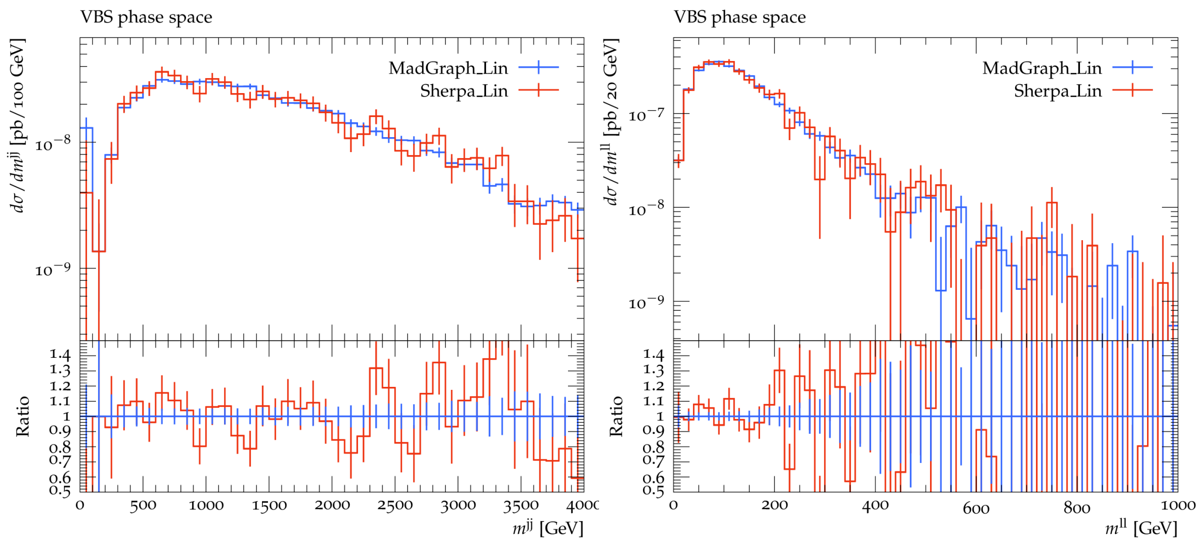

Figure 4.22: Comparison between the linear contributions produced with the SMEFTsim model in MadGraph and Sherpa. The histograms show the differential distributions of the invariant masses of the two jets (left) and the two leptons (right).

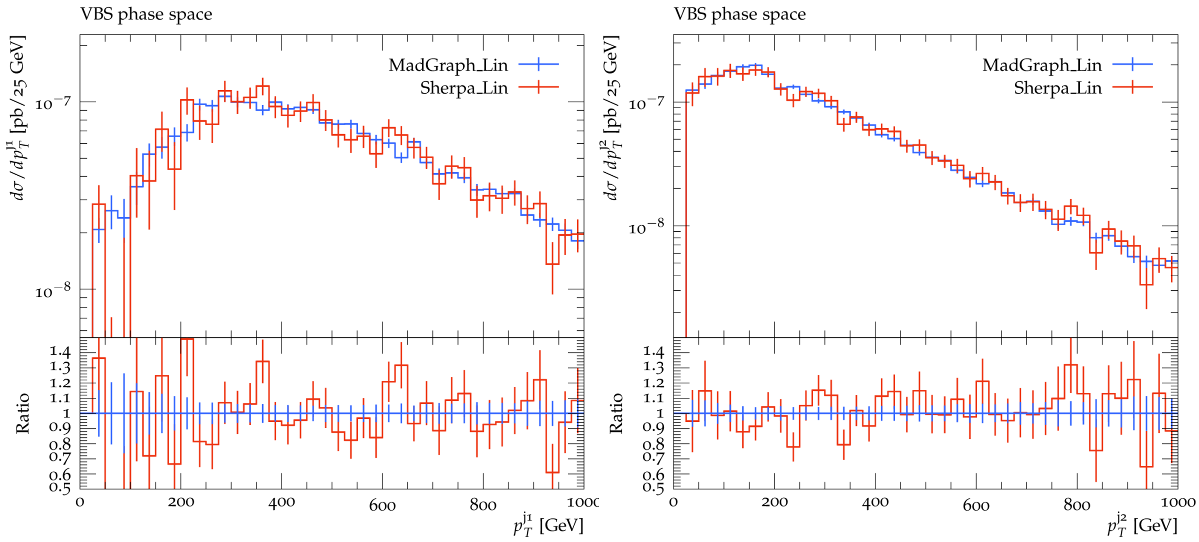

Figure 4.23: Comparison between the linear contributions produced with the SMEFTsim model in MadGraph and Sherpa. The histograms show the differential distributions of the transverse momenta of the leading jet (left) and the subleading jet (right).

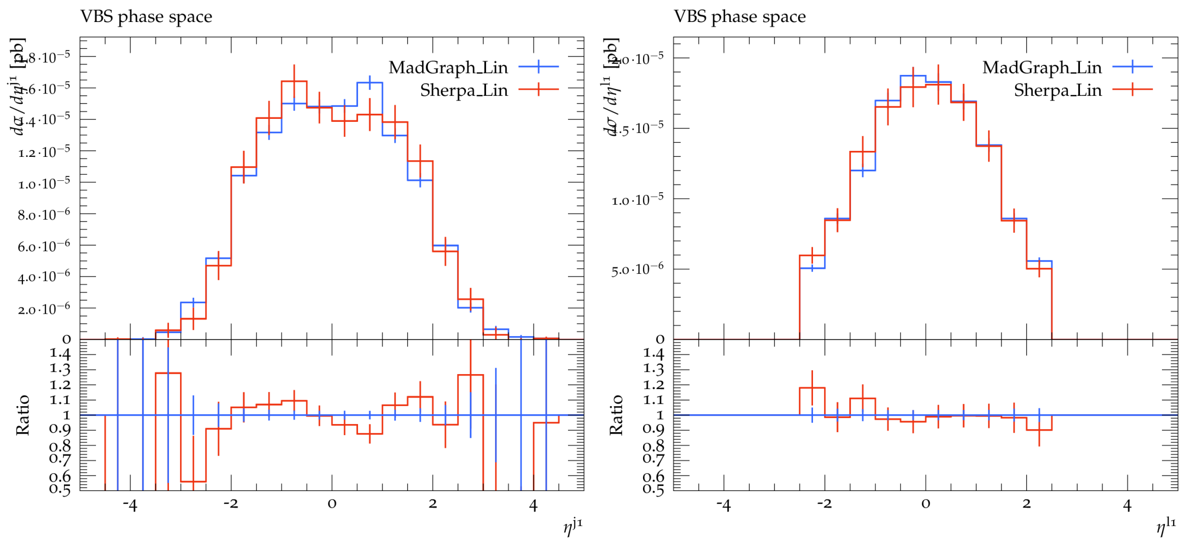

Figure 4.24: Comparison between the linear contributions produced with the SMEFTsim model in MadGraph and Sherpa. The histograms show the differential distributions of the transverse momenta of the leading jet (left) and the subleading jet (right).

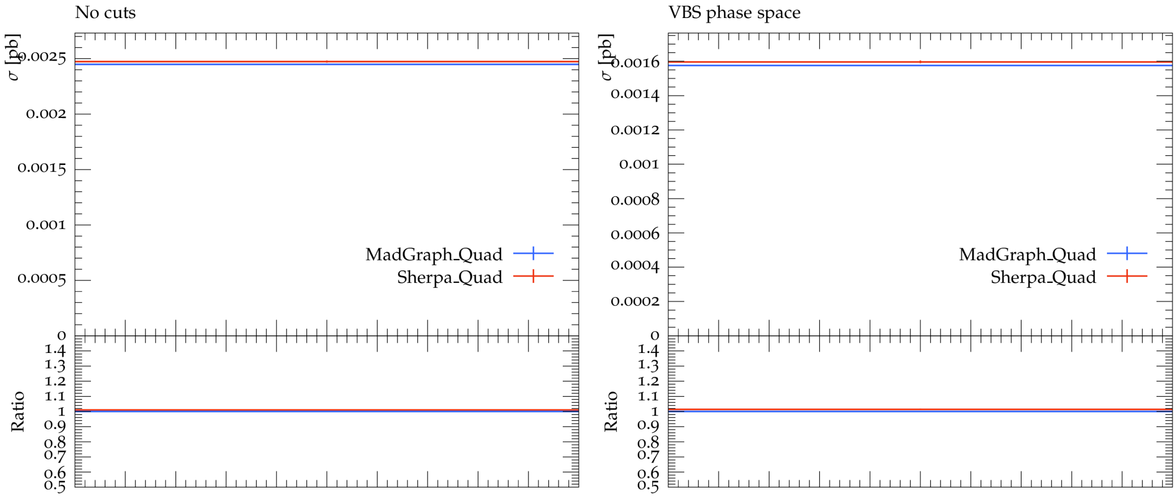

Figure 4.25: Comparison between the quadratic contributions produced with the SMEFTsim model in MadGraph and Sherpa. The plots show the total cross-section before (left) and after (right) the VBS analysis cuts.

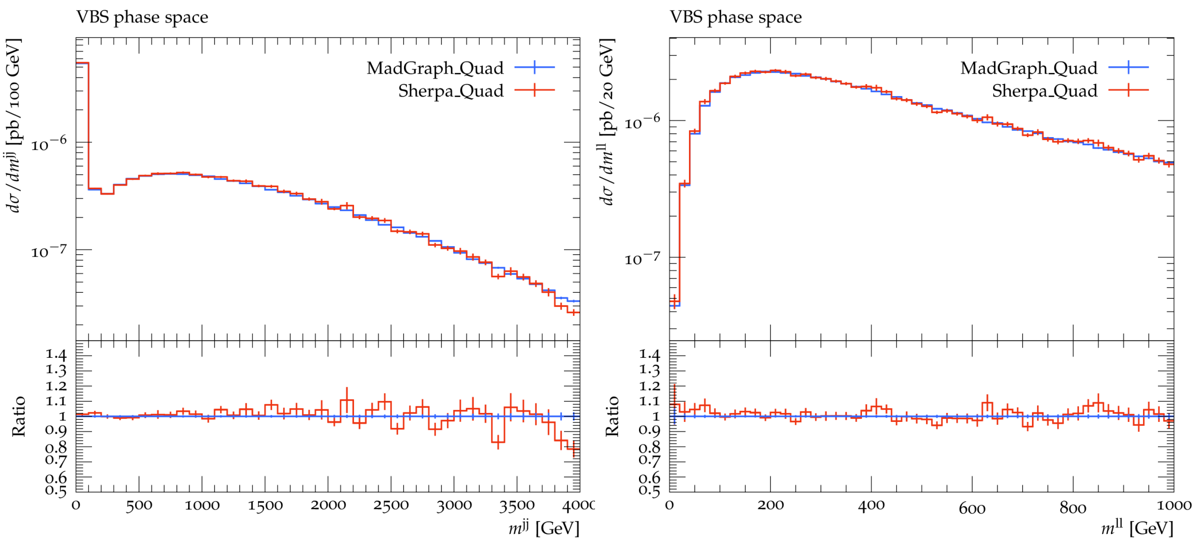

Figure 4.26: Comparison between the quadratic contributions produced with the SMEFTsim model in MadGraph and Sherpa. The histograms show the differential distributions of the invariant masses of the two jets (left) and the two leptons (right).

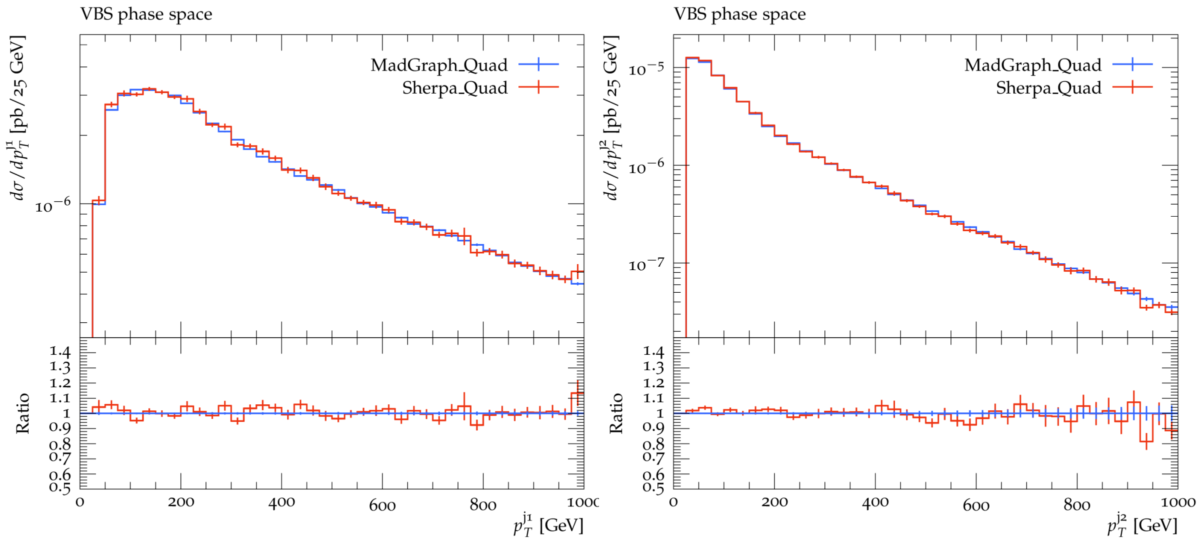

Figure 4.27: Comparison between the quadratic contributions produced with the SMEFTsim model in MadGraph and Sherpa. The histograms show the differential distributions of the transversal momenta of the leading (left) and subleading (right) jets.

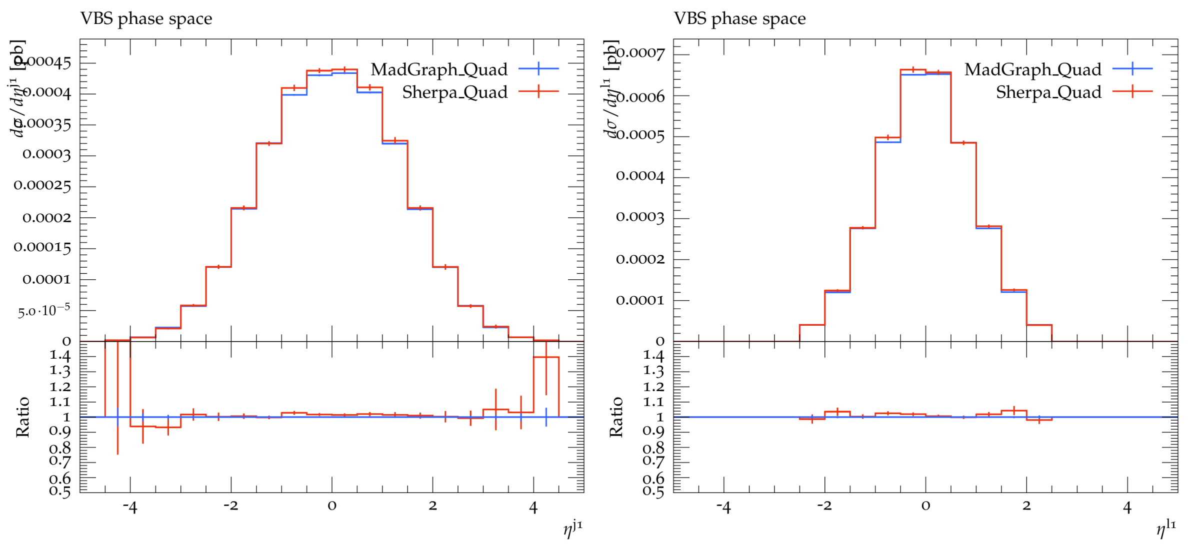

Figure 4.28: Comparison between the quadratic contributions produced with the SMEFTsim model in MadGraph and Sherpa. The histograms show the differential distributions of the pseudorapidities of the leading jet (left) and the leading lepton (right).

5 Validation using the HHVBF_UFO model

This second set of validation tests uses a different model in order to diversify the testing scenarios. As described in [4], the HHVBF_UFO model gives the user access to three parameters named `CV`, `C2V` and `C3`. They alter the strengths of the Higgs to two vector bosons, two Higgs to one vector boson and triple Higgs couplings, respectively, and are defined to be equal to one in the case of the SM. The process described in section 2.2.2 includes diagrams with both triple-Higgs vertices and vertices with two vector bosons and one Higgs boson. The diagram shown in figure 2.3 also includes the decay of both W bosons and the Higgs bosons into stable particles. The VBS process for the SMEFTsim validation was defined by the initial and final state particles of the desired signal process. In the case of the triple Higgs coupling process however, the contribution of the targeted diagram to the full process specified by the initial and final state particles would be so small that the impact of the adjusted Higgs coupling would likely be very hard to see. Both MadGraph and Sherpa offer syntax that would allow the user to require the presence of two W bosons and one Higgs boson, and to control their decay channels. However, specifying the decays in this way is handled differently in Sherpa and MadGraph and would introduce an additional layer of complexity, which is not related to the use of the UFO model and therefore does not contribute to the intended validation. That is why, in the interest of limiting the scope of this project, the final state of the events generated for this validation consists of two W bosons, one Higgs boson and two quarks. In a real experimental scenario, the bosons would decay before reaching the detector and the down quarks would be registered as hadronic jets, whose kinematic properties would need to be constructed in a complex clustering process. That means that the plots shown in this section are quite far removed from experimental reality and are only meant to aid in the technical validation process.

5.1 Event Generation and Rivet Analysis

All samples produced for the following tests contain either 500,000 unweighted MadGraph events or 10 million weighted Sherpa events. The settings used for the event generation are summarized in table 5.1. Just like in the event generation with the SMEFTsim model, the interaction order for QCD interactions was set to zero for all samples in both Sherpa and MadGraph. As in the SMEFTsim validation, all uncertainties are statistical.

The Rivet analysis used for these tests was built for this project and is very rudimentary. It simply accesses the particles and their properties from the event generation's final state and plots them. Even the down quarks are accessed directly without any clustering algorithm being used. The analysis does not include any cuts. As in the analysis used for the SMEFTsim validation, the results are scaled using $\frac{\sigma}{\sum_i w_i}$.

Table 5.1: Settings for the generation of events using the HHVBF_UFO model in Sherpa and MadGraph.

General Settings: Variable	Value
Renormalization Scale	100 GeV
Beam Energy	6500 GeV
PDF set	PDF4LHC21_40_pdfas
Generation Level Cuts	
Minimum Jet p_t	20 GeV
Minimum ΔR for jets	0.4
Maximum $\lvert\eta_j\rvert$	5
m_τ	1.777 GeV
m_t	172 GeV
m_Z	91.1876 GeV
m_W	80.384 85 GeV
m_H	125 GeV
m_d,m_u,m_s,m_c, m_e, m_μ,m_b	0
width Z	2.4952 GeV
width W	2.085 GeV
width top	1.508 336 GeV
width H	0.0041 GeV
SM inputs for UFO	
α_s	determined by PDF
aEWM1	132.233
G_f	$1.166\,378\,7 \times 10^{-5}\,\mathrm{GeV}^{-2}$
Specific to Sherpa:	
process definition	2 2 -> 24 24 25 1 1
for built-in SM: EW input scheme	Gmu
Specific to MadGraph	
Process Definition	u u > w+ w+ h d d

5.2 Validation Results

Four validation tests are performed using the HHVBF_UFO model. The first is equivalent to section 4.3.1 and compares the SM limit of the UFO model to Sherpa's built-in SM. In the second step, the UFO's SM limit in Sherpa is compared to the same sample produced with MadGraph. Finally, the comparison between Sherpa and MadGraph is repeated for samples with an altered triple-Higgs coupling and Higgs-and-two-vector-boson coupling.

5.2.1 Comparing Sherpa's SM and the SM limit of HHVBF_UFO

The comparison between Sherpa's built-in SM and the SM limit of the UFO model does not show good agreement between the two samples. This is already visible in the integrated cross-sections, with $\sigma_{\text{Sherpa\_SM}} = 0.1508(4)\,\text{fb}$ for Sherpa's built-in SM and $\sigma_{\text{UFO\_SM}} = 0.1340(4)\,\text{fb}$ for the UFO's SM limit. The differential distributions in figures 5.1, 5.2, 5.3 and 5.4 confirm this discrepancy. There appear to be both a constant scaling factor and differences in shape between the samples. The scaling factor can be identified through an approximately constant offset in the ratio plot. It appears to be present in all the distributions, but it is most clearly visible in the plots that do not show an apparent shape difference, like the pseudorapidities depicted in figure 5.3 and the invariant mass of the two down quarks in figure 5.1. The remaining plots all show a shape difference in addition to the scaling factor. The difference in shape becomes more pronounced with rising energy.

The reason for this mismatch could not be determined within the time-frame of this project. The next step in learning more about its cause could be to simplify the process even further, or to restrict the included diagrams using the interaction order syntax until a direct comparison of the individual diagrams is feasible. As with the SMEFTsim example, some settings like the SM input scheme cannot be directly translated from the UFO to Sherpa's built-in SM. Varying these input parameters could be a way to estimate the effect those necessary differences have on the final results. Another step to further investigate this issue could be to repeat this comparison in MadGraph, i.e. to compare MadGraph's built-in SM to the SM limit of the UFO model. This could help to ensure that all of the UFO's settings are used correctly. In order to investigate the scaling factor and the shape differences independently, a normalized version of the histograms could be used.

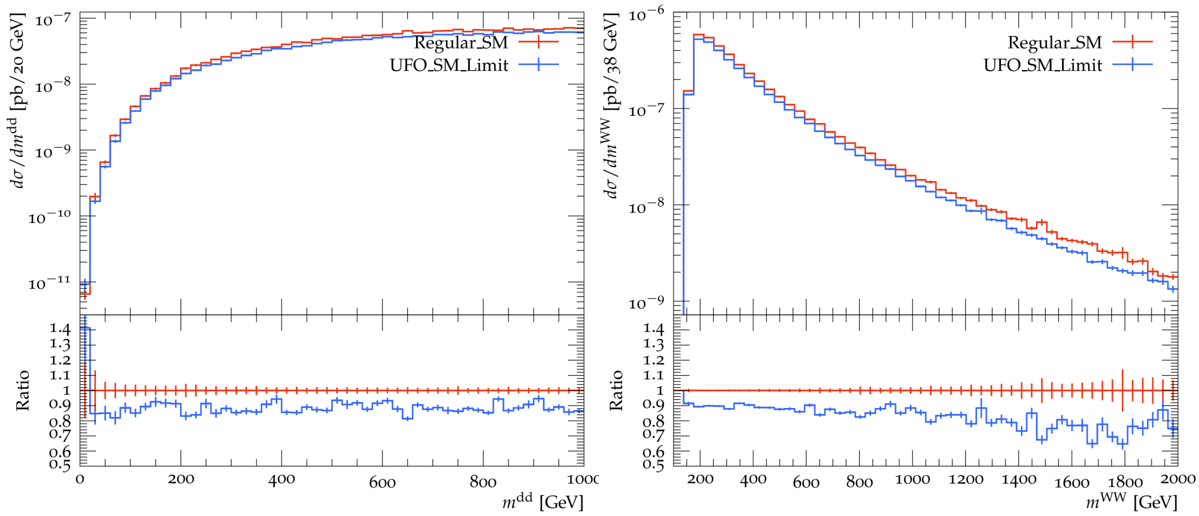

Figure 5.1: Comparison between the sample generated using Sherpa's built-in SM and the sample generated with the SM limit of the HHVBF_UFO model. The histograms show the differential distributions for the invariant masses of the two down quarks (left) and the two W bosons (right).

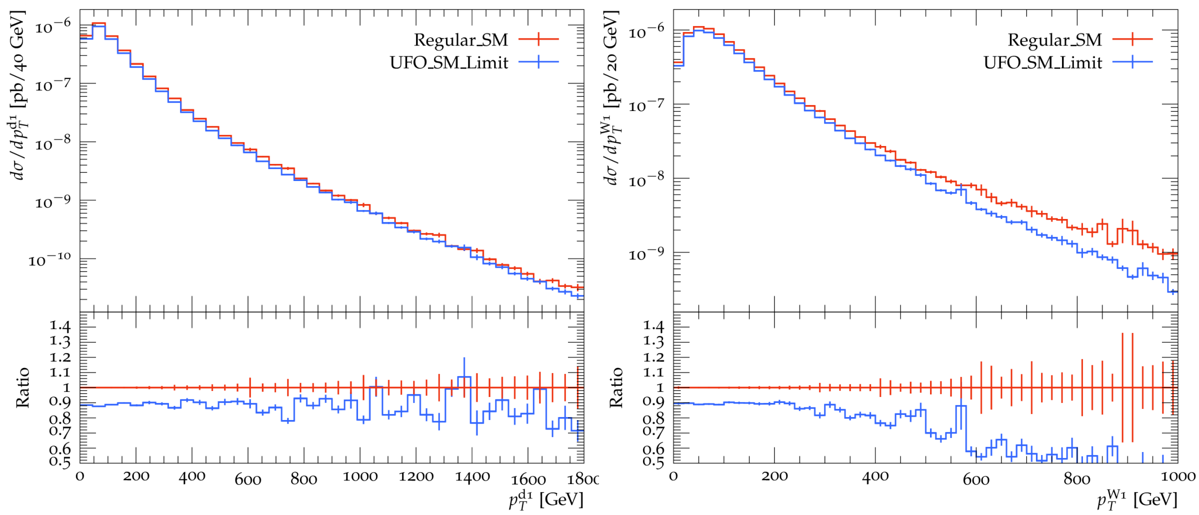

Figure 5.2: Comparison between the sample generated using Sherpa's built-in SM and the sample generated with the SM limit of the HHVBF_UFO model. The histograms show the differential distributions for the transverse momenta of the leading down quark (left) and the leading W boson (right).

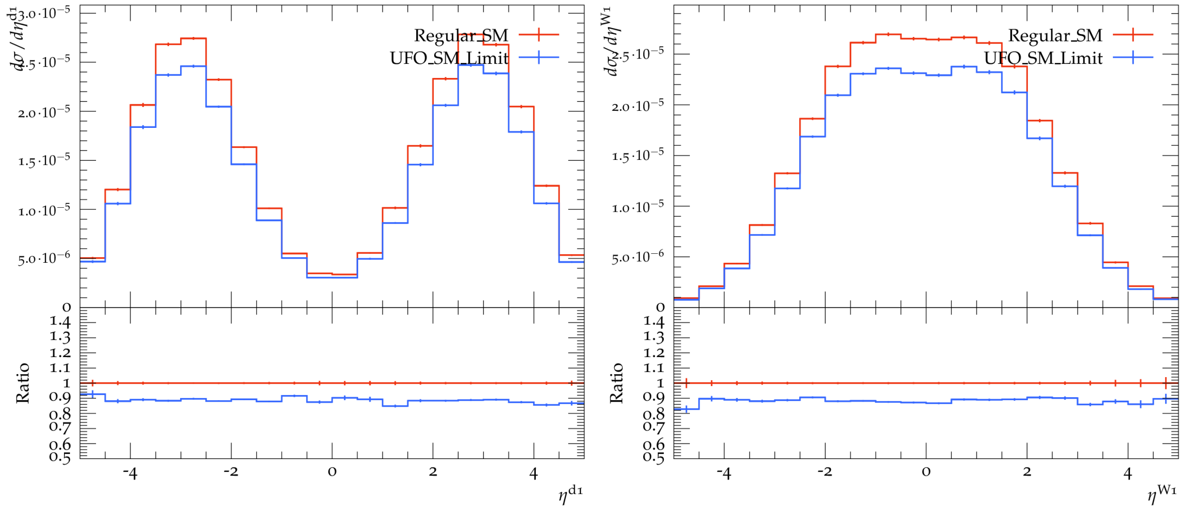

Figure 5.3: Comparison between the sample generated using Sherpa's built-in SM and the sample generated with the SM limit of the HHVBF_UFO model. The histograms show the differential distributions for the pseudorapidities of the leading down quark (left) and the leading W boson (right).

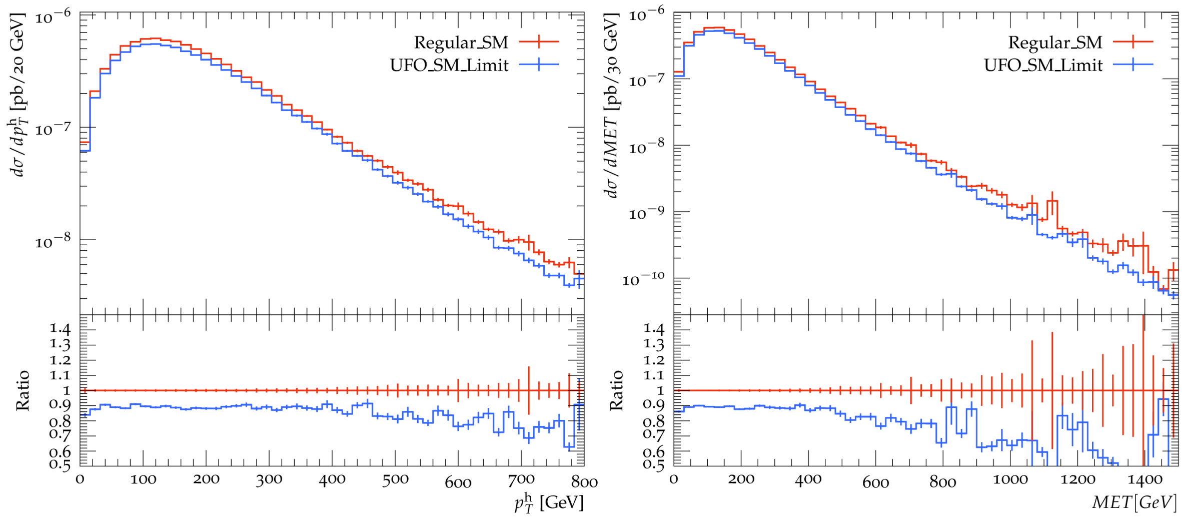

Figure 5.4: Comparison between the sample generated using Sherpa's built-in SM and the sample generated with the SM limit of the HHVBF_UFO model. The histograms show the differential distributions for the transverse momentum of the higgs boson (left) and the missing transverse energy (right).

5.2.2 Comparing MadGraph and Sherpa: SM

The second test performed using the HHVBF_UFO model is a comparison between the model's SM limit in MadGraph and Sherpa. The total cross-sections for these two samples imply that the agreement is not perfect here either: $\sigma_{\text{Sherpa}} = 0.1340(4)$ fb for the Sherpa sample and $\sigma_{\text{MadGraph}} = 0.1308(5)$ fb for the MadGraph sample. Figures 5.5, 5.6, 5.3 and 5.4 show that while there appears to be a much smaller scaling difference between the differential cross-sections in comparison to the SM case, there is still noticeable shape differences. There is a very clear difference at high energies in the invariant mass of the two W bosons in figure 5.5 and the leading W boson's transverse momentum in figure 5.6. The higher uncertainties in the case of the leading down quark's momentum make the assessment more difficult, but there is no clear shape in the invariant mass of the two down quarks in figure 5.5. There is a clear shape difference in the pseudorapidity of the leading W boson, as shown in figure 5.7. The differential cross-section for high values of $|\eta^{\text{W1}}|$ is clearly lower in the MadGraph sample than in the Sherpa sample. While the agreement is better for the transverse momentum of the Higgs boson and the missing transverse energy in figure 5.8 than in the case of the SM, the histograms still show visible shape differences. The reason for these discrepancies could not be determined during the course of this thesis. A possible next step could be the generation of more unweighted MadGraph events, in order to decrease the statistical uncertainties in the histograms that show the down quarks' characteristics. Knowing whether and how much they are affected as well could provide insight into the cause of the shape differences. Apart from that, switching to a different process with another final state could be helpful in determining what kind of final state particles are affected. Solving this problem would be a high priority in further validating this UFO model, since the model does not have the ability to differentiate between BSM contributions like SMEFTsim does. This means that all tests with non-SM parameters will also be affected by these differences.

5.2.3 Comparing MadGraph and Sherpa: Altered Triple-Higgs Coupling

After having compared the SM samples, the `c3` parameter is set to `c3 = 10`, altering the triple Higgs coupling. This results in a slightly increased total cross-section of $\sigma_{\text{Sherpa}} = 0.1796(6)$ fb in the Sherpa sample and $\sigma_{\text{MadGraph}} = 0.1775(6)$ fb in the MadGraph sample. As these still do not agree within one standard deviation, some differences between the Sherpa and MadGraph samples in the differential distributions are to be expected. In

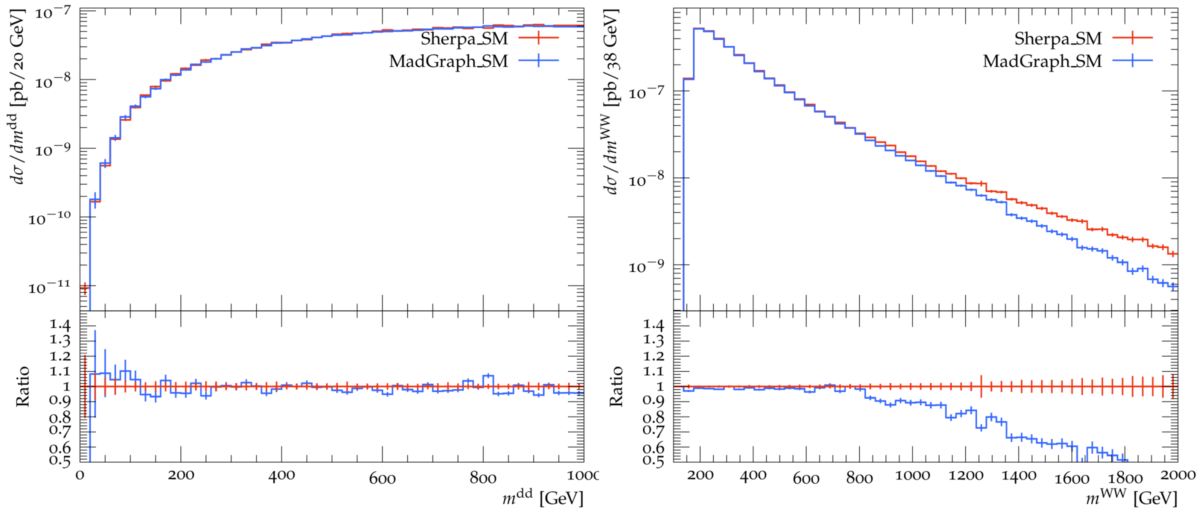

Figure 5.5: Comparison between the samples generated in MadGraph and Sherpa using the SM limit of the HHVBF_UFO model. The histograms show the differential distributions for the invariant masses of the two down quarks (left) and the two W bosons (right).

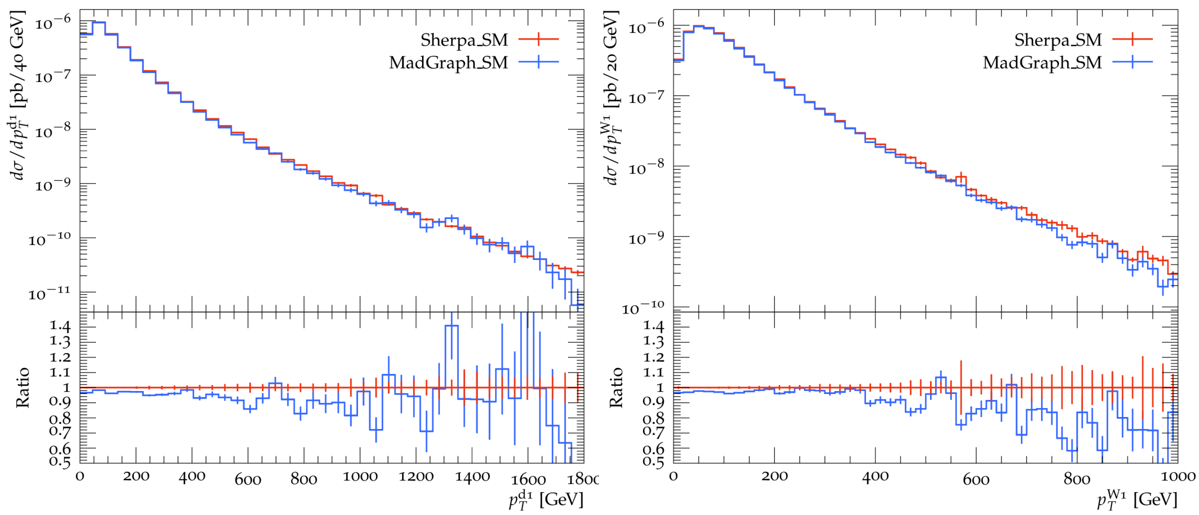

Figure 5.6: Comparison between the samples generated in MadGraph and Sherpa using the SM limit of the HHVBF_UFO model. The histograms show the differential distributions for the transverse momentum of the leading down quark (left) and the leading W boson (right).

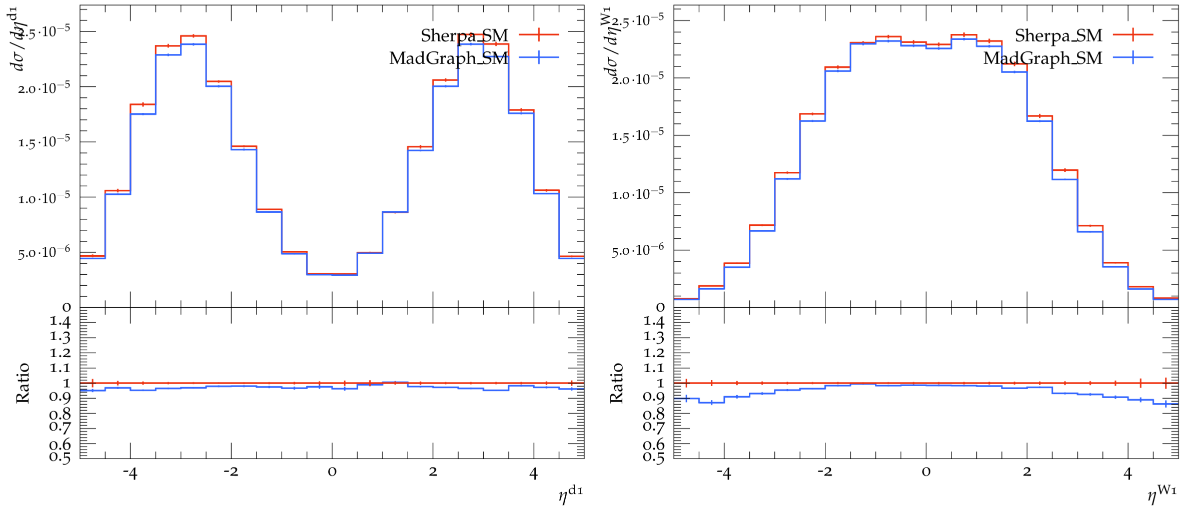

Figure 5.7: Comparison between the samples generated in MadGraph and Sherpa using the SM limit of the HHVBF_UFO model. The histograms show the differential distributions for the pseudorapidities of the leading down quark (left) and the leading W boson (right).

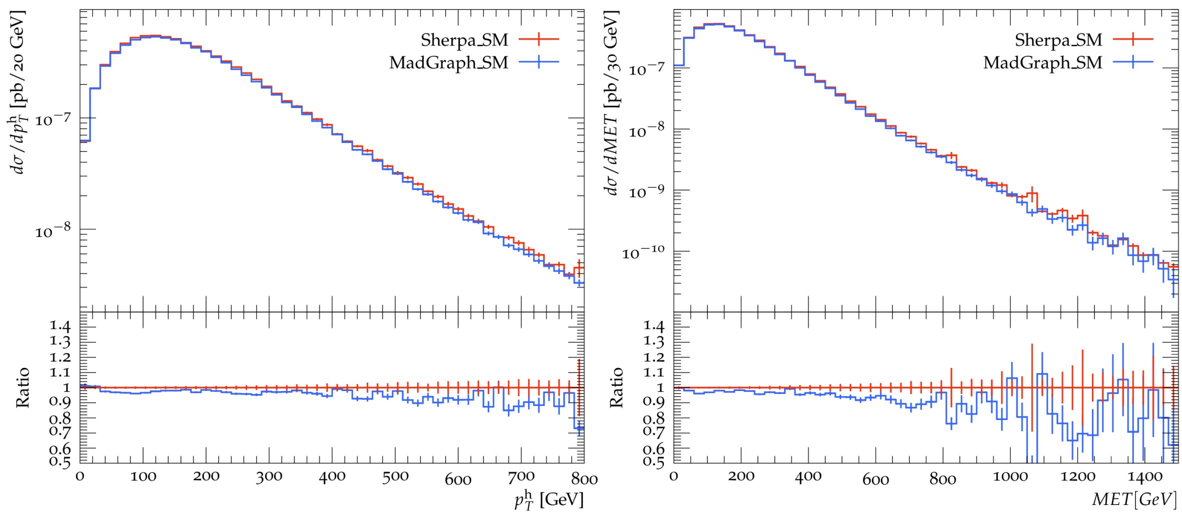

Figure 5.8: Comparison between the samples generated in MadGraph and Sherpa using the SM limit of the HHVBF_UFO model. The histograms show the differential distributions for the transverse momentum of the Higgs boson (left) and the missing transverse energy(right).

contrast to the comparison between MadGraph and Sherpa in the SM case, there is no apparent scaling factor between the two samples. As in the SM case, the most pronounced difference in shape is visible in the distribution of the invariant mass of the two W bosons in figure 5.9. Without the scaling factor there is now good agreement for the invariant mass of the two down quarks. There is a difference in shape for the transverse momentum of the leading down quark in figure 5.10 at energies around 800 GeV, but due to the large uncertainties in the high-energy tail of the distribution the shape difference can no longer be accurately assessed. The same is true for the differential distribution of the leading W boson's transverse momentum. While there is a clear shape difference in the pseudorapidity of the leading W boson in figure 5.11, the difference is much smaller for the pseudorapidity of the leading down quark. It is difficult to assess whether the Higgs bosons transverse momentum and the missing transverse energy in figure 5.12 exhibit any shape differences due to the large uncertainties at high energies.
Overall the BSM samples show similar shape differences as the SM samples, but in some distributions they are less pronounced. A possible interpretation could be that the shape differences do not increase with the cross-section, which means that in the case of the slightly larger cross-section of the BSM sample the differences are less significant.

5.2.4 Comparing MadGraph and Sherpa: Altered Higgs-Vector-Boson Coupling

The hypothesis of the shape differences not growing with the cross-section is supported by this next test, in which the `cv` parameter is set to `cv = 2`. The resulting total cross-sections of $\sigma_{\text{Sherpa}} = 0.0617(8)\,\text{pb}$ for the Sherpa sample and $\sigma_{\text{MadGraph}} = 0.062\,23(22)\,\text{pb}$ in the MadGraph sample are much larger than the corresponding SM cross-sections. As figures 5.13, 5.14 and 5.16 show, the shape differences are no longer visible in most plots. The only exception is the pseudorapidity of the leading W boson in figure 5.15, which might still show differences at the tails of the distribution. A histogram with more events and therefore smaller uncertainties would help to confirm this observation.
As mentioned above, the disappearance of the shape differences in this test might be due to the much larger cross-sections. If the discrepancies are caused by an effect that does not grow with the cross-section, the differences might be very small in comparison to the increased cross-section.

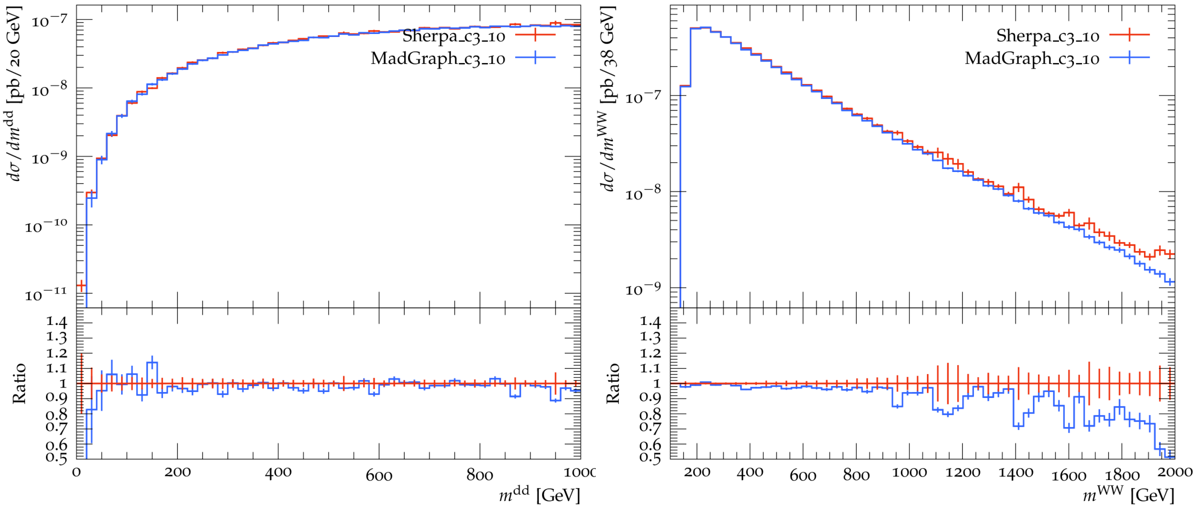

Figure 5.9: Comparison between the samples generated in MadGraph and Sherpa using the HHVBF_UFO model with an altered triple Higgs coupling ($c3 = 10$). The histograms show the differential distributions for the invariant masses of the two down quarks (left) and the two W bosons (right).

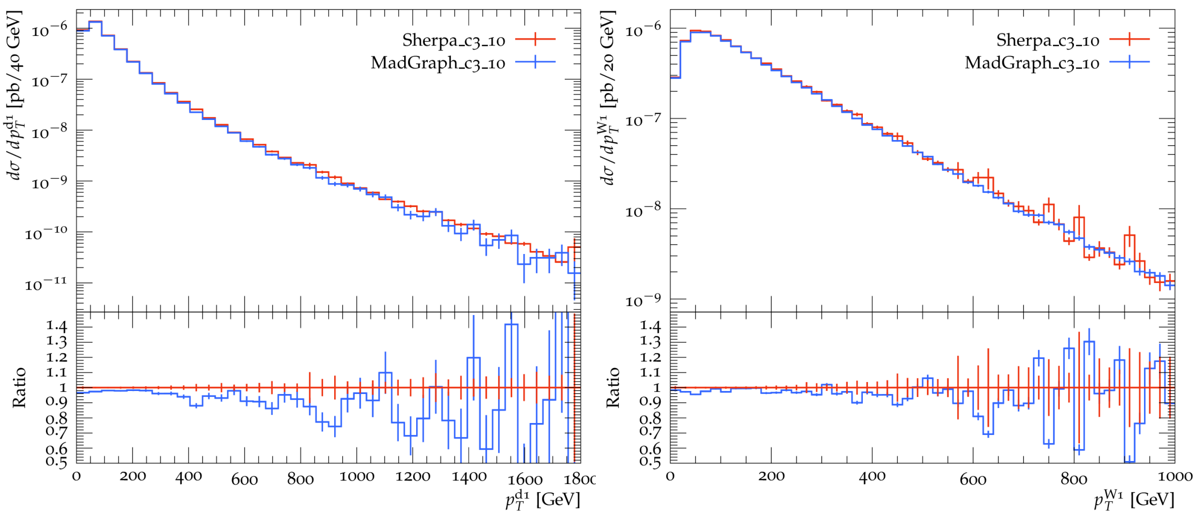

Figure 5.10: Comparison between the samples generated in MadGraph and Sherpa using the HHVBF_UFO model with an altered triple Higgs coupling ($c3 = 10$). The histograms show the differential distributions for the transverse momenta of the leading down quark (left) and the leading W bosons (right).

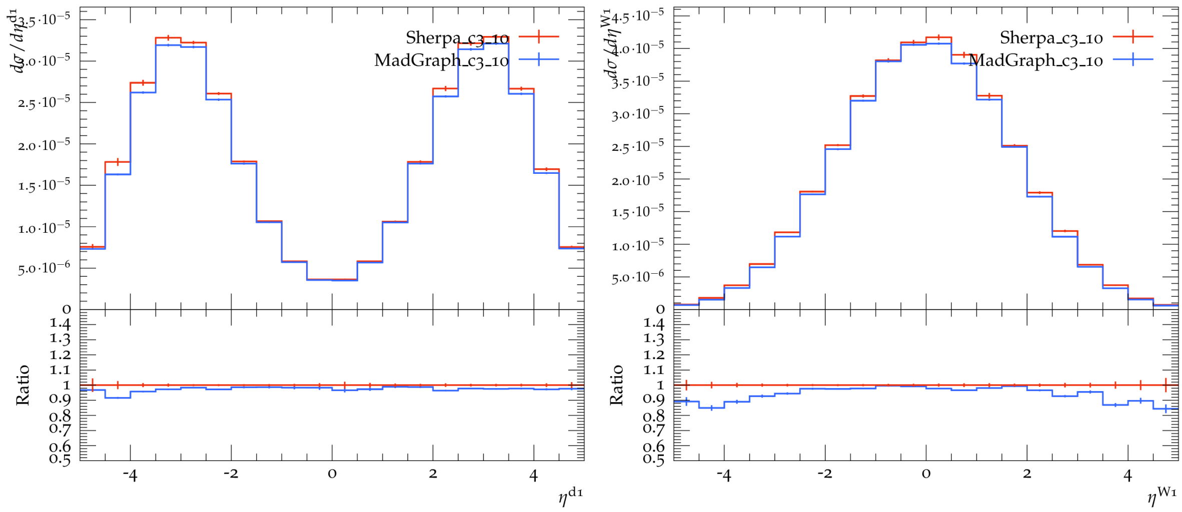

Figure 5.11: Comparison between the samples generated in MadGraph and Sherpa using the HHVBF_UFO model with an altered triple Higgs coupling ($c3 = 10$). The histograms show the differential distributions for the transverse momenta of the leading down quark (left) and the leading W bosons (right).

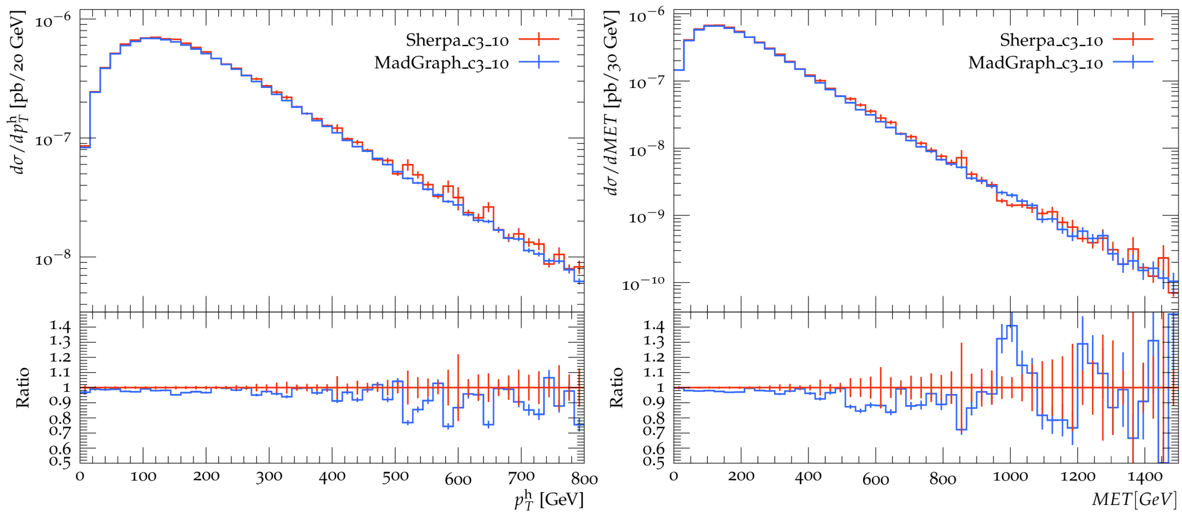

Figure 5.12: Comparison between the samples generated in MadGraph and Sherpa using the HHVBF_UFO model with an altered triple Higgs coupling ($c3 = 10$). The histograms show the differential distributions for the transverse momentum of the Higgs boson (left) and the missing transverse energy (right).

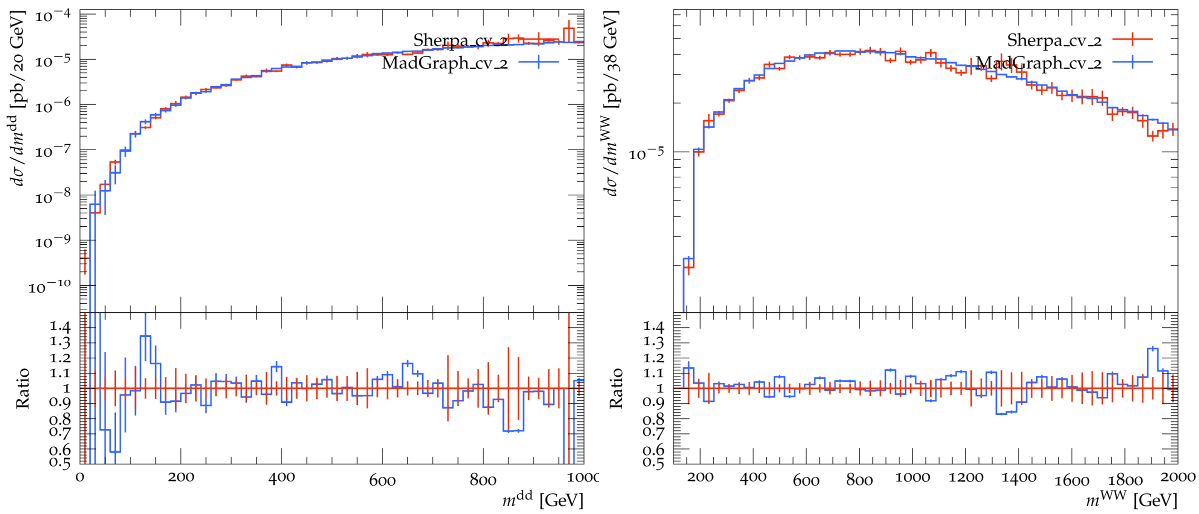

Figure 5.13: Comparison between the samples generated in MadGraph and Sherpa using the HHVBF_UFO model with an altered coupling for vertices including one Higgs and two vector bosons ($cv = 2$). The histograms show the differential distributions for the inverse masses of the two down quarks (left) and the two W bosons (right).

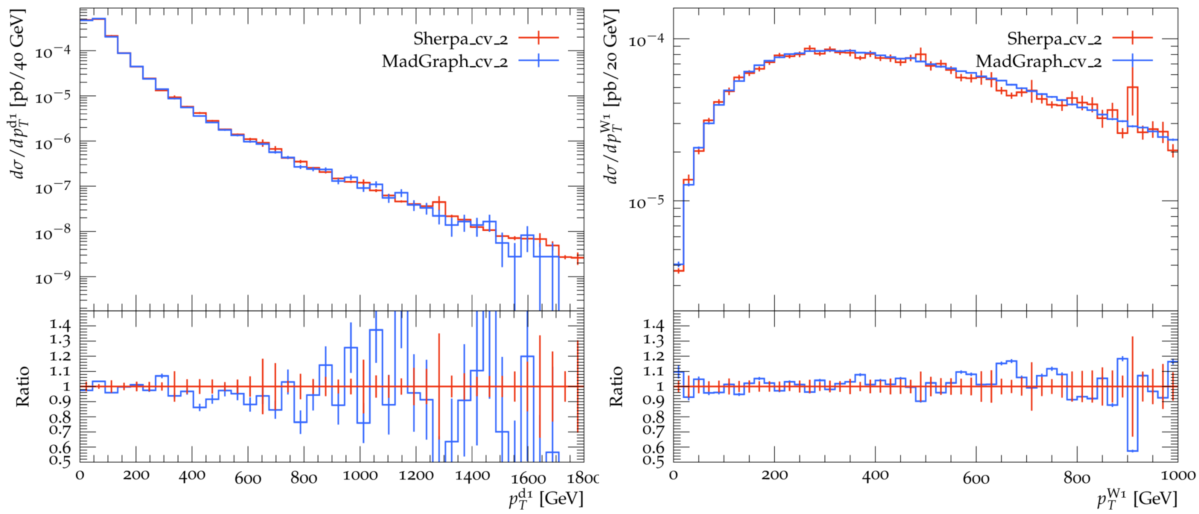

Figure 5.14: Comparison between the samples generated in MadGraph and Sherpa using the HHVBF_UFO model with an altered coupling for vertices including one Higgs and two vector bosons ($cv = 2$). The histograms show the differential distributions for the transverse momenta of the leading down quark (left) and the leading W boson (right).

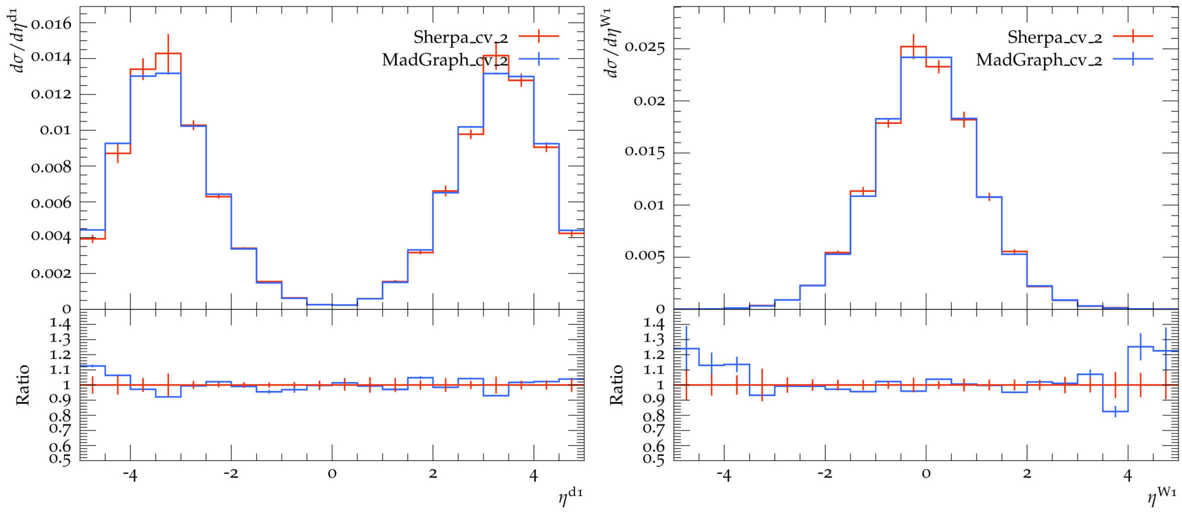

Figure 5.15: Comparison between the samples generated in MadGraph and Sherpa using the HHVBF_UFO model with an altered coupling for vertices including one Higgs and two vector bosons ($cv = 2$). The histograms show the differential distributions for the pseudorapidities of the leading down quark (left) and the leading W boson (right).

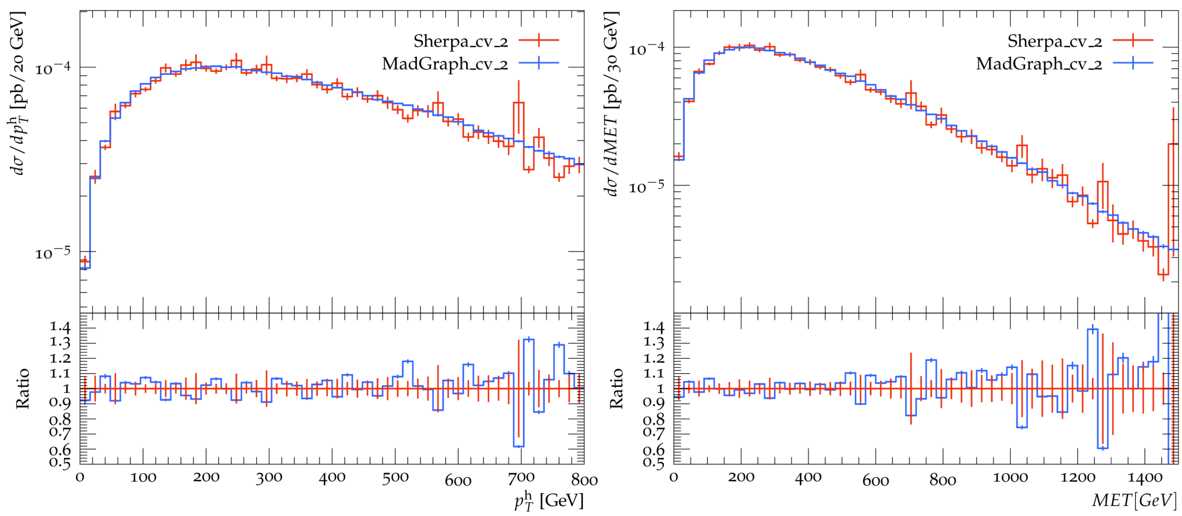

Figure 5.16: Comparison between the samples generated in MadGraph and Sherpa using the HHVBF_UFO model with an altered coupling for vertices including one Higgs and two vector bosons ($cv = 2$). The histograms show the differential distributions for the transverse momentum of the Higgs boson (left) and the missing transverse energy (right).

6 Conclusion and Outlook

Two different models have been used to validate Sherpa's ability to generate events based on UFO models. The validation based on the SMEFTsim model was performed in two ways: by checking the consistency of the results within Sherpa and by comparing them to events generated with MadGraph. The results of the Sherpa-internal validation show good agreement between Sherpa's built-in SM and the SM limit of the UFO model. Two tests for the decomposition method were performed. The first, consisting of a comparison between a sample produced without decomposition and the sum of the individual contributions, showed good agreement. The second test included the reconstruction of the linear and quadratic contributions from two samples without decomposition and with opposite-sign Wilson coefficients. The results showed that this test is more conclusive for contributions that are not too small in comparison to the samples without decomposition, since otherwise the uncertainties are so large in relation to the reconstructed contribution that a shape comparison is difficult. This means that while the results for the reconstructed linear contribution can only rule out an extreme mismatch, the results for the quadratic reconstruction showed good agreement between the reconstructed contribution and the individually generated sample.

The comparison with MadGraph also showed good agreement, with the exception of a noticeable shape difference in transverse momenta of the jets in the SM contribution. The reason for this mismatch could not be ascertained.

The results for the validation of the HHVBF_UFO model were less clear. Especially the mismatch between Sherpa's built-in SM and the SM limit of the UFO model suggests that the settings used to produce the two samples were not understood well enough. The shape differences in the comparison with MadGraph appeared to become less pronounced as the cross-section grew with the alteration of the coupling parameters. This could suggest that the issue could be resolved for all values of the BSM parameters once good agreement is achieved in the SM case. A more detailed investigation would be needed to learn more about the disagreement, including for example a simpler process definition or the plotting of additional variables.

Due to time constraints, the inclusion of a second UFO model in the testing was prioritized over the detailed testing of all of SMEFTsim's capabilities. This means that there are features like propagator corrections or corrections to loop-generated Higgs interactions that could be the target of additional tests of Sherpa's usage of SMEFTsim. Similarly, the tests using the HHVBF_UFO model only included a variation of the Higgs-two-vector-boson vertex via `CV` and the triple-Higgs vertex via `C3`. Further tests could be done by changing the third available coupling (two-higgs-one-vector-boson). Generally speaking, the validation tests in this thesis show that when using a UFO model, it is advisable to perform at least a couple of consistency checks to ensure a good understanding of the settings and syntax options involved.

One way to further validate Sherpa's interaction with UFO models overall would be to test additional models, preferably with a more diverse physics content. The validations performed in this thesis were focused on the electroweak sector of the SM and (to a lesser degree) the Higgs sector and their BSM extensions. This means that one possible avenue for further testing could involve a model that alters the QCD sector of the SM. The validations performed in this thesis were based mostly on the comparison with MadGraph. Another way to extend the testing would be to compare the result to additional event generators. One possibility could be HERWIG, which also has the ability to utilize UFO models.

Bibliography

[1] Enrico Bothmann et al. "Event generation with Sherpa 2.2". In: *SciPost Physics* 7.3 (Sept. 2019). DOI: 10.21468/scipostphys.7.3.034. URL: https://doi.org/10.21468%2Fscipostphys.7.3.034.

[2] Céline Degrande et al. "UFO – The Universal FeynRules Output". In: *Computer Physics Communications* 183.6 (2012), pp. 1201–1214. ISSN: 0010-4655. DOI: https://doi.org/10.1016/j.cpc.2012.01.022. URL: https://www.sciencedirect.com/science/article/pii/S0010465512000379.

[3] Ilaria Brivio, Yun Jiang and Michael Trott. "The SMEFTsim package, theory and tools". In: *Journal of High Energy Physics* 2017.12 (2017). ISSN: 1029-8479. DOI: 10.1007/jhep12(2017)070. URL: http://dx.doi.org/10.1007/JHEP12(2017)070.

[4] Fady Bishara, Roberto Contino and Juan Rojo. "Higgs pair production in vector-boson fusion at the LHC and beyond". In: *The European Physical Journal C* 77.7 (July 2017). DOI: 10.1140/epjc/s10052-017-5037-9. URL: https://doi.org/10.1140%2Fepjc%2Fs10052-017-5037-9.

[5] J. Alwall et al. "The automated computation of tree-level and next-to-leading order differential cross sections, and their matching to parton shower simulations". In: *Journal of High Energy Physics* 2014.7 (July 2014). DOI: 10.1007/jhep07(2014)079. URL: https://doi.org/10.1007%2Fjhep07%282014%29079.

[6] ATLAS Collaboration. "The ATLAS Experiment at the CERN Large Hadron Collider". In: *Journal of Instrumentation* 3.08 (Aug. 2008), S08003–S08003. ISSN: 1748-0221. DOI: 10.1088/1748-0221/3/08/S08003. URL: https://iopscience.iop.org/article/10.1088/1748-0221/3/08/S08003 (visited on 31/10/2023).

[7] The CMS Collaboration. "The CMS experiment at the CERN LHC". In: *Journal of Instrumentation* 3.08 (Aug. 2008), S08004. DOI: 10.1088/1748-0221/3/08/S08004. URL: https://dx.doi.org/10.1088/1748-0221/3/08/S08004.

[8] *The Large Hadron Collider*. Dec. 2023. URL: https://home.cern/science/accelerators/large-hadron-collider (visited on 06/12/2023).

[9] The ATLAS Collaboration. "Observation of a new particle in the search for the Standard Model Higgs boson with the ATLAS detector at the LHC". In: *Physics Letters B* 716.1 (2012), pp. 1–29. ISSN: 0370-2693. DOI: https://doi.org/10.1016/j.physletb.2012.08.020. URL: https://www.sciencedirect.com/science/article/pii/S037026931200857X.

[10] Christian Bierlich et al. *A comprehensive guide to the physics and usage of PYTHIA 8.3*. 2022. arXiv: 2203.11601 [hep-ph].

[11] Stefan Höche et al. "Beyond Standard Model calculations with Sherpa". In: *Eur. Phys. J. C* 75.3 (2015), p. 135. DOI: 10.1140/epjc/s10052-015-3338-4. arXiv: 1412.6478 [hep-ph].

[12] A. Einstein. "Die Grundlage der allgemeinen Relativitätstheorie". In: *Annalen der Physik* 354.7 (1916), pp. 769–822. DOI: https://doi.org/10.1002/andp.19163540702. URL: https://onlinelibrary.wiley.com/doi/abs/10.1002/andp.19163540702.

[13] Gordon Kane. *Modern Elementary Particle Physics*. 2nd ed. Cambridge University Press, 2017.

[14] E. Noether. "Invariante Variationsprobleme". In: *Nachrichten von der Gesellschaft der Wissenschaften zu Göttingen, Mathematisch-Physikalische Klasse* 1918 (1918), pp. 235–257. URL: http://eudml.org/doc/59024.

[15] R. L. Workman et al. "Review of Particle Physics". In: *PTEP* 2022 (2022), p. 083C01. DOI: 10.1093/ptep/ptac097.

[16] C. S. Wu et al. "Experimental Test of Parity Conservation in Beta Decay". In: *Phys. Rev.* 105 (4 Feb. 1957), pp. 1413–1415. DOI: 10.1103/PhysRev.105.1413. URL: https://link.aps.org/doi/10.1103/PhysRev.105.1413.

[17] F. Englert and R. Brout. "Broken Symmetry and the Mass of Gauge Vector Mesons". In: *Phys. Rev. Lett.* 13 (9 Aug. 1964), pp. 321–323. DOI: 10.1103/PhysRevLett.13.321. URL: https://link.aps.org/doi/10.1103/PhysRevLett.13.321.

[18] Peter W. Higgs. "Spontaneous Symmetry Breakdown without Massless Bosons". In: *Phys. Rev.* 145 (4 May 1966), pp. 1156–1163. DOI: 10.1103/PhysRev.145.1156. URL: https://link.aps.org/doi/10.1103/PhysRev.145.1156.

[19] Mark Thomson. *Modern Particle Physics*. Cambridge University Press, 2015.

[20] Steven Weinberg. “Baryon- and Lepton-Nonconserving Processes”. In: *Phys. Rev. Lett.* 43 (21 Nov. 1979), pp. 1566–1570. DOI: 10.1103/PhysRevLett.43.1566. URL: https://link.aps.org/doi/10.1103/PhysRevLett.43.1566.

[21] B. Grzadkowski et al. “Dimension-Six Terms in the Standard Model Lagrangian”. In: *Journal of High Energy Physics* 2010.10 (Oct. 2010). arXiv:1008.4884 [hep-ph], p. 85. ISSN: 1029-8479. DOI: 10.1007/JHEP10(2010)085. URL: http://arxiv.org/abs/1008.4884 (visited on 25/10/2023).

[22] Tyler Corbett, O. J. P. Eboli and M. C. Gonzalez-Garcia. “Unitarity Constraints on Dimension-Six Operators”. In: *Physical Review D* 91.3 (Feb. 2015). arXiv:1411.5026 [hep-ph], p. 035014. ISSN: 1550-7998, 1550-2368. DOI: 10.1103/PhysRevD.91.035014. URL: http://arxiv.org/abs/1411.5026 (visited on 25/10/2023).

[23] Rodrigo Alonso et al. “Renormalization Group Evolution of the Standard Model Dimension Six Operators III: Gauge Coupling Dependence and Phenomenology”. In: *Journal of High Energy Physics* 2014.4 (Apr. 2014). arXiv:1312.2014 [hep-ph], p. 159. ISSN: 1029-8479. DOI: 10.1007/JHEP04(2014)159. URL: http://arxiv.org/abs/1312.2014 (visited on 25/10/2023).

[24] *Combined effective field theory interpretation of Higgs boson and weak boson production and decay with ATLAS data and electroweak precision observables*. Tech. rep. Geneva: CERN, 2022. URL: https://cds.cern.ch/record/2816369.

[25] Ondřej Penc and on behalf of the ATLAS collaboration. “Observation and measurements of vector-boson scattering with the ATLAS detector”. In: *Physica Scripta* 95.8 (July 2020), p. 084014. ISSN: 1402-4896. DOI: 10.1088/1402-4896/aba0f6. URL: https://iopscience.iop.org/article/10.1088/1402-4896/aba0f6 (visited on 03/11/2023).

[26] Benjamin W. Lee, C. Quigg and H. B. Thacker. “The Strength of Weak Interactions at Very High-Energies and the Higgs Boson Mass”. In: *Phys. Rev. Lett.* 38 (1977), pp. 883–885. DOI: 10.1103/PhysRevLett.38.883.

[27] ATLAS Collaboration. “Observation of Electroweak Production of a Same-Sign W Boson Pair in Association with Two Jets in p p Collisions at s = 13 TeV with the ATLAS Detector”. In: *Physical Review Letters* 123.16 (Oct. 2019), p. 161801. ISSN: 0031-9007, 1079-7114. DOI: 10.1103/PhysRevLett.123.161801. URL: https://link.aps.org/doi/10.1103/PhysRevLett.123.161801 (visited on 31/10/2023).

[28] CMS Collaboration. "Observation of Electroweak Production of Same-Sign W Boson Pairs in the Two Jet and Two Same-Sign Lepton Final State in Proton-Proton Collisions at s = 13 TeV". In: *Physical Review Letters* 120.8 (Feb. 2018), p. 081801. ISSN: 0031-9007, 1079-7114. DOI: 10.1103/PhysRevLett.120.081801. URL: https://link.aps.org/doi/10.1103/PhysRevLett.120.081801 (visited on 31/10/2023).

[29] Michael Rauch. *Vector-Boson Fusion and Vector-Boson Scattering*. 2016. arXiv: 1610.08420 [hep-ph].

[30] Pankaj Agrawal et al. "Determining the Shape of Higgs Potential at Future Colliders". In: *Physical Review D* 101.7 (Apr. 2020). arXiv:1907.02078 [hep-ex, physics:hep-ph], p. 075023. ISSN: 2470-0010, 2470-0029. DOI: 10.1103/PhysRevD.101.075023. URL: http://arxiv.org/abs/1907.02078 (visited on 31/10/2023).

[31] Brian Henning et al. "Measuring Higgs Couplings without Higgs Bosons". In: *Physical Review Letters* 123.18 (Oct. 2019). DOI: 10.1103/physrevlett.123.181801. URL: https://doi.org/10.1103%2Fphysrevlett.123.181801.

[32] *The history of CERN | timeline.web.cern.ch*. URL: https://timeline.web.cern.ch/timeline-header/89 (visited on 20/11/2023).

[33] Lyndon Evans and Philip Bryant. "LHC Machine". In: *Journal of Instrumentation* 3.08 (Aug. 2008), S08001. DOI: 10.1088/1748-0221/3/08/S08001. URL: https://dx.doi.org/10.1088/1748-0221/3/08/S08001.

[34] *First beam in the LHC - accelerating science*. Nov. 2023. URL: https://home.cern/news/press-release/cern/first-beam-lhc-accelerating-science (visited on 20/11/2023).

[35] "Collider halted until next year". In: (Sept. 2008). URL: http://news.bbc.co.uk/2/hi/in_depth/7632408.stm (visited on 06/12/2023).

[36] Mike Lamont. "The First Years of LHC Operation for Luminosity Production". In: (2013), MOYAB101. URL: https://cds.cern.ch/record/2010134.

[37] *Long Shutdown 1: Exciting times ahead*. Dec. 2023. URL: https://home.web.cern.ch/news/news/accelerators/long-shutdown-1-exciting-times-ahead (visited on 06/12/2023).

[38] *LHC Season 2: holding the key to new frontiers*. Nov. 2023. URL: https://home.cern/news/news/accelerators/lhc-season-2-holding-key-new-frontiers (visited on 20/11/2023).

[39] *A successful conclusion to Run 2*. Nov. 2023. URL: https://home.cern/news/opinion/accelerators/successful-conclusion-run-2 (visited on 20/11/2023).

[40] *LHC upgrades during LS2*. Dec. 2023. URL: https://home.cern/press/2022/lhc-upgrades-during-ls2 (visited on 06/12/2023).

[41] *Run 3: an opportunity to expand the LHC physics programme*. Dec. 2023. URL: https://home.cern/press/2022/run-3 (visited on 06/12/2023).

[42] *High-Luminosity LHC*. Dec. 2023. URL: https://home.cern/science/accelerators/high-luminosity-lhc (visited on 06/12/2023).

[43] Ewa Lopienska. "The CERN accelerator complex, layout in 2022. Complexe des accélérateurs du CERN en janvier 2022". In: (2022). General Photo. URL: https://cds.cern.ch/record/2800984.

[44] Riccardo Maria Bianchi and ATLAS Collaboration. "ATLAS experiment schematic illustration". General Photo. 2022. URL: https://cds.cern.ch/record/2837191.

[45] *Trigger and Data Acquisition System*. URL: https://atlas.cern/Discover/Detector/Trigger-DAQ (visited on 06/12/2023).

[46] *Model Data Base – FeynRules*. URL: http://feynrules.irmp.ucl.ac.be/wiki/ModelDatabaseMainPage (visited on 03/12/2023).

[47] Christian Bierlich et al. "Robust Independent Validation of Experiment and Theory: Rivet version 3". In: *SciPost Physics* 8.2 (Feb. 2020). ISSN: 2542-4653. DOI: 10.21468/scipostphys.8.2.026. URL: http://dx.doi.org/10.21468/SciPostPhys.8.2.026.

[48] Ilaria Brivio. "SMEFTsim 3.0 – a practical guide". In: *Journal of High Energy Physics* 2021.4 (Apr. 2021). arXiv:2012.11343 [hep-ex, physics:hep-ph], p. 73. ISSN: 1029-8479. DOI: 10.1007/JHEP04(2021)073. URL: http://arxiv.org/abs/2012.11343 (visited on 04/10/2023).

[49] *Home - VBSCan COST Network*. URL: https://vbscanaction.web.cern.ch/ (visited on 02/12/2023).

[50] *Sherpa 3.0.0 Manual — Sherpa Manual 3.0.0 documentation*. URL: https://sherpa-team.gitlab.io/sherpa/master/index.html (visited on 02/12/2023).

List of Figures

Erklärung

Hiermit erkläre ich, dass ich diese Arbeit im Rahmen der Betreuung am Institut für Kern- und Teilchenphysik ohne unzulässige Hilfe Dritter verfasst und alle Quellen als solche gekennzeichnet habe.

Maren Bühring
Dresden, 07.11.2023